



Search for pair-produced scalar and vector leptoquarks decaying into third-generation quarks and first- or second-generation leptons in pp collisions with the ATLAS detector

The ATLAS Collaboration

A search for pair-produced scalar and vector leptoquarks decaying into quarks and leptons of different generations is presented. It uses the full LHC Run 2 (2015–2018) data set of 139 fb^{-1} collected with the ATLAS detector in proton–proton collisions at a centre-of-mass energy of $\sqrt{s} = 13 \text{ TeV}$. Scalar leptoquarks with charge $-(1/3)e$ as well as scalar and vector leptoquarks with charge $+(2/3)e$ are considered. All possible decays of the pair-produced leptoquarks into quarks of the third generation (t, b) and charged or neutral leptons of the first or second generation (e, μ, ν) with exactly one electron or muon in the final state are investigated. No significant deviations from the Standard Model expectation are observed. Upper limits on the production cross-section are provided for eight models as a function of the leptoquark mass and the branching ratio of the leptoquark into the charged or neutral lepton. In addition, lower limits on the leptoquark masses are derived for all models across a range of branching ratios. Two of these models have the goal of providing an explanation for the recent B -anomalies. In both models, a vector leptoquark decays into charged and neutral leptons of the second generation with a similar branching fraction. Lower limits of 1980 GeV and 1710 GeV are set on the leptoquark mass for these two models.

Contents

1	Introduction	2
2	ATLAS detector	4
3	Data and simulated event samples	4
4	Event reconstruction	6
5	Event selection and categorisation	8
6	Neural network training	11
7	Systematic uncertainties	13
8	Statistical interpretation	14
9	Results	15
10	Conclusion	22

1 Introduction

Recent hints of a potential violation of lepton flavour universality in various measurements of B -meson decays (' B -anomalies') [1–9] can be attributed, if confirmed, to the exchange of leptoquarks (LQs) [10–18]. In addition, some of these models introducing LQs aim to simultaneously provide an explanation for the longstanding discrepancy between the measured and the predicted anomalous magnetic moment of the muon [19]. LQs have already been discussed for a few decades, as they are predicted by many extensions of the Standard Model (SM), e.g. in unified theories [20–22] and technicolor [23–25] or composite models [26–28]. LQs provide a connection between the quark and lepton sectors, which exhibit similar structures. They are bosons carrying colour charge and fractional electrical charge. LQs possess non-zero baryon and lepton numbers and are assumed to decay into a quark–lepton pair. The branching ratio into a quark and a charged lepton is denoted by \mathcal{B} , and that into a quark and neutrino by $1 - \mathcal{B}$. Leptoquarks can be scalar or vector bosons and can be produced singly or in pairs in proton–proton collisions.

The assumption that LQs can only interact with leptons and quarks of the same generation [29], and are spin-0 particles, has been used in most of the searches for LQs. Recently, however, searches for LQs with couplings to quarks and leptons of different generations have aroused interest because these couplings are required in order to explain the B -anomalies mentioned above. In particular, the theoretical explanations usually require LQs with couplings to third-generation quarks and second-generation leptons. Similarly, vector LQs with a charge of $2/3$, in units of the elementary charge e , have been identified recently as promising candidates [30, 31].

First results of searches for LQs with couplings to quarks and leptons of different generations were published recently for pair-produced LQs decaying into charged leptons, i.e. in dilepton final states. Results from the full LHC Run 2 data set (2015–2018) of proton–proton collisions at $\sqrt{s} = 13$ TeV collected by ATLAS, corresponding to an integrated luminosity of 139 fb^{-1} , are available for pair-produced scalar LQs decaying

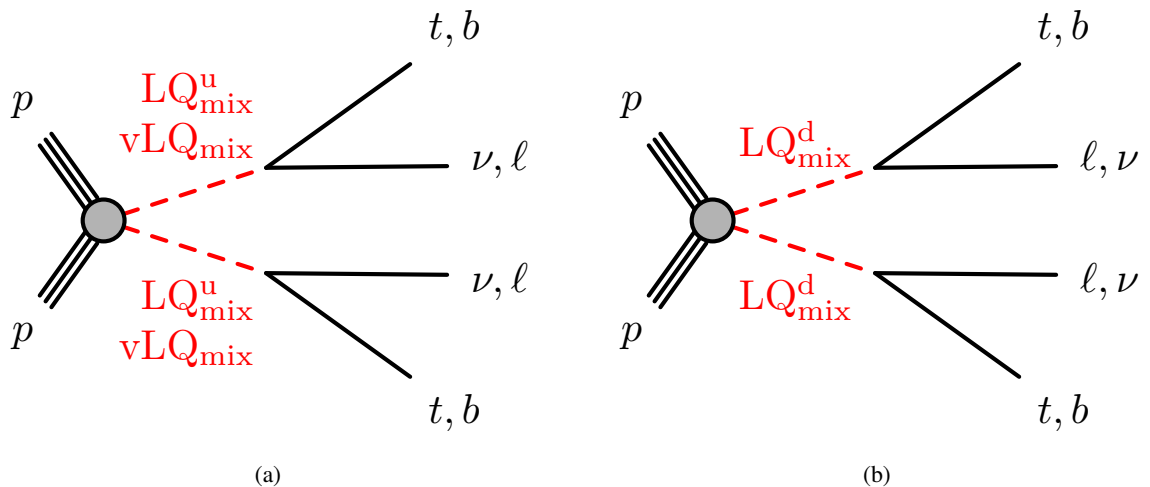


Figure 1: Pair production and decay of (a) up-type scalar (LQ_{mix}^u) and vector (vLQ_{mix}) LQs and (b) down-type scalar (LQ_{mix}^d) LQs with $\ell = e, \mu$. No distinction is made between particles and antiparticles.

into a top-quark and an electron or muon [32] and for the decay into a b -, c - or light-quark and an electron or muon [33]. The CMS Collaboration has published a search for pair-produced LQs decaying into a top-quark and a muon using a partial (35.9 fb^{-1}) Run 2 data set [34] where, in addition, results for vector LQs were derived by scaling the results for scalar LQs to the larger production cross-sections expected for vector LQs, assuming no kinematic differences.

Given the good coverage of large branching ratios \mathcal{B} by the dileptonic measurements described above, the results presented here use a single-lepton (electron or muon) final state optimised for medium to small \mathcal{B} . In this case, one of the LQs decays into a neutrino and the other decays into a charged lepton, or both decay into neutrinos and the charged lepton arises from a leptonically decaying top-quark (t_{lep}). The results are interpreted as searches for pair-produced LQs with charges of either $\pm(2/3)e$ (up-type) or $\pm(1/3)e$ (down-type). All possible decays of the pair-produced up-type and down-type LQs into a quark (t, b) of the third generation and a lepton (ℓ, ν) of the first or second generation are considered, as seen in Figure 1. With flavour off-diagonal couplings allowed, the model used for up-type (LQ_{mix}^u) and down-type (LQ_{mix}^d) scalar LQs is an extension of that [35] used in previous ATLAS searches [36], where all possible decays of the pair-produced up-type and down-type scalar LQs into a quark (t, b) and a lepton (τ, ν) of the third generation were considered. The present search for up-type LQs is also optimised for a vector LQ (vLQ) model [37] designed to provide an explanation for the various B -anomalies.

The analysis strategy is based on a final-state signature with one lepton, high missing transverse momentum and at least four jets due to a hadronically decaying top-quark (t_{had}) and a b -quark. Dedicated neural networks (NNs), trained in a common training region, are used for the separation of signal and background. This is done separately for scalar and vector LQ pair-production because they exhibit different kinematic behaviour for small values of \mathcal{B} , i.e. when the charged lepton arises mostly from the top-quark decay. For each of the models and for various branching ratios, a signal region (SR) based on the NN output is defined. Control regions (CRs) are defined so as to be enriched in the various background processes. They are orthogonal to the SR, and orthogonal to each other. The statistical interpretation is based on a simultaneous fit to the CRs and the SR, in which the background normalisations and a possible signal contribution are determined, while taking into account the experimental and theoretical systematic uncertainties. The

results are presented as limits on the leptoquark mass as a function of the branching ratio.

2 ATLAS detector

The ATLAS experiment [38] at the LHC is a multipurpose particle detector with a forward–backward symmetric cylindrical geometry and a near 4π coverage in solid angle.¹ It consists of an inner tracking detector surrounded by a thin superconducting solenoid providing a 2 T axial magnetic field, electromagnetic and hadron calorimeters, and a muon spectrometer. The inner tracking detector (ID) covers the pseudorapidity range $|\eta| < 2.5$. It consists of silicon pixel, silicon microstrip, and transition radiation tracking detectors. Lead/liquid-argon (LAr) sampling calorimeters provide electromagnetic (EM) energy measurements with high granularity. A steel/scintillator-tile hadron calorimeter covers the central pseudorapidity range ($|\eta| < 1.7$). The endcap and forward regions are instrumented with LAr calorimeters for both the EM and hadronic energy measurements up to $|\eta| = 4.9$. The muon spectrometer (MS) surrounds the calorimeters and is based on three large superconducting air-core toroidal magnets with eight coils each. The field integral of the toroids ranges between 2.0 and 6.0 Tm across most of the detector. The muon spectrometer includes a system of precision tracking chambers and fast detectors for triggering. A two-level trigger system is used to select events. The first-level trigger is implemented in hardware and uses a subset of the detector information to accept events at a rate below 100 kHz. This is followed by a software-based trigger that reduces the accepted event rate to 1 kHz on average depending on the data-taking conditions. An extensive software suite [39] is used in the reconstruction and analysis of real and simulated data, in detector operations, and in the trigger and data acquisition systems of the experiment.

3 Data and simulated event samples

In this search, data from proton–proton collisions at $\sqrt{s} = 13$ TeV corresponding to an integrated luminosity of 139 fb^{-1} , collected in the years 2015 to 2018 with the ATLAS detector, are analysed. Data are required to have been collected during stable beam conditions and with all detector subsystems operational [40]. The average number of simultaneous pp interactions per bunch crossing, referred to as pile-up, is approximately 34, averaged over the whole data set.

Monte Carlo (MC) simulated event samples are used to model the signal and background processes. In all samples except those produced with SHERPA 2.2.1 or SHERPA 2.2.2 [41], decays of heavy-flavour hadrons were modelled with EVTGEN 1.2.0 or EVTGEN 1.6.0 [42], depending on the process. Pile-up was modelled by overlaying minimum-bias events generated with PYTHIA 8.186 [43] and the A3 [44] set of tuned parameters (referred to as the ‘tune’) onto the simulated hard-scatter events. A reweighting procedure was applied in order to match the pile-up profile of the recorded data. The ATLAS simulation infrastructure [45] was used to simulate the detector and its response. Nominal SM background samples were produced with a detailed GEANT4 [46] detector simulation, whereas a faster calorimeter simulation [45] was applied for the signal samples and systematic variations of the backgrounds. The same offline reconstruction methods

¹ ATLAS uses a right-handed coordinate system with its origin at the nominal interaction point (IP) in the centre of the detector and the z -axis along the beam pipe. The x -axis points from the IP to the centre of the LHC ring, and the y -axis points upwards. Cylindrical coordinates (r, ϕ) are used in the transverse plane, ϕ being the azimuthal angle around the z -axis. The pseudorapidity is defined in terms of the polar angle θ as $\eta = -\ln \tan(\theta/2)$. Angular distance is measured in units of $\Delta R \equiv \sqrt{(\Delta\eta)^2 + (\Delta\phi)^2}$.

used for data were applied to the simulated samples. Corrections were applied to the simulated events in order to match the selection efficiencies and energy and mass scales and resolutions of reconstructed simulated particles to those measured in data control samples.

Simulated events with pair-produced scalar LQs were generated at next-to-leading order (NLO) in quantum chromodynamics (QCD) with MADGRAPH5_AMC@NLO 2.6.0 [47] and the NNPDF3.0_{NLO} parton distribution function (PDF) [48] set with $\alpha_s = 0.118$. An extension of the LQ model of Ref. [35] was used, allowing flavour off-diagonal couplings. The model is based on previous fixed-order NLO QCD calculations [49, 50]. To retain information about spin correlations, the decays of LQs as well as top-quarks were handled with MADSPIN [51]. MADGRAPH5_AMC@NLO was interfaced with PYTHIA 8.230 [52] to model the parton shower (PS), hadronisation, and underlying event (UE). Here and in the following, PYTHIA was used with the A14 tune [53] and the NNPDF2.3_{LO} [54] set of PDFs. The coupling strength λ was set to 0.3. The model parameter $\beta \in [0, 1]$ modifies the coupling of LQs to leptons, such that the coupling to charged leptons is given by $\sqrt{\beta}\lambda$ and to neutrinos by $\sqrt{1 - \beta}\lambda$. It differs from the branching fraction \mathcal{B} into charged leptons because of phase-space corrections arising mainly from the large top-quark mass. The parameter β was set to 0.5 in the simulation. Different values for \mathcal{B} were achieved by reweighting the MC events according to their decay, as described in Ref. [36]. The LQ pair-production cross-sections were obtained from the calculation of direct top-squark pair production, as this process has the same production modes, computed at approximate next-to-next-to-leading order (NNLO) in QCD with resummation of next-to-next-to-leading logarithmic (NNLL) soft gluon terms [55–58]. The cross-sections do not include lepton t -channel contributions, which are neglected in Ref. [35] and may lead to corrections at the percent level [59]. For this analysis, signal samples were produced separately for electrons and muons and for both up- and down-type LQs with a mass spacing of 100 GeV from 300 GeV to 800 GeV and from 1600 GeV to 2500 GeV, and with a finer spacing of 50 GeV between 800 GeV and 1600 GeV to improve the resolution around the expected mass exclusion limit.

Simulated events with pair-produced up-type vector LQs were generated at leading order (LO) in QCD with MADGRAPH5_AMC@NLO 2.8.1 and the NNPDF3.0_{NLO} PDF set with $\alpha_s = 0.118$. Decays of the vLQs and top-quarks were handled with MADSPIN, while the PS and hadronisation were simulated with PYTHIA 8.244. The U_1 vLQ model in Ref. [37] is used for the muon channel, directly seeking an explanation for the various B -anomalies. Couplings to electrons are assumed to vanish in this model because of existing tight bounds from low-energy observables, mainly in the lepton-flavour-violating sector. Nevertheless, an extension of the model [60] was used in this analysis to also probe the electron channel. The samples were produced with a coupling strength of $g_U = 3.0$. The large value of g_U is motivated by a suppression of the production cross-section for additional mediators in an ultraviolet-complete model, which might otherwise be in tension with existing LHC limits. The model accommodates both left- and right-handed couplings to fermions, where in the case of only left-handed couplings the coupling strengths to charged leptons and neutrinos are equal ($\beta = 0.5$). Although only left-handed couplings were used in producing the MC samples, the analysis uses the same reweighting of MC events as in the scalar LQ case to also probe different values of \mathcal{B} . The model allows use of either the minimal (vLQ_{mix}^{min}) or the Yang–Mills (vLQ_{mix}^{YM}) coupling scenario, where in the latter the vLQ is a heavy gauge boson resulting in enhanced cross-sections. Kinematic differences between the minimal and the Yang–Mills coupling scenario were found to be negligible, except for masses below about 500 GeV. Samples were produced separately for the two coupling scenarios and for both muons and electrons, with a mass spacing of 100 GeV from 300 GeV to 1400 GeV and from 2300 GeV to 2500 GeV, and with a finer spacing of 50 GeV between 1400 GeV and 2300 GeV. No higher-order cross-section computations are available for this model. Therefore, the cross-sections computed at leading order by MADGRAPH5_AMC@NLO are used in the analysis.

Dominant background processes in the search include top-quark pair ($t\bar{t}$), W +jets and single top-quark production, the last being mainly associated production of a top-quark and W boson (tW). In addition, $t\bar{t}+V$ ($V = W, Z$), diboson, $t\bar{t}+H$, and Z +jets processes are also considered in the analysis. Contributions from multi-jet background with a jet misidentified as a lepton are negligible in the phase space of interest.

The production of $t\bar{t}$ events was modelled using the POWHEG BOX [61–64] v2 generator at NLO with the NNPDF3.0_{NLO} set of PDFs and the h_{damp} parameter² set to $1.5 m_t$ [65]. The cross-section was corrected to the theory prediction at NNLO including resummation of NNLL soft-gluon terms calculated using TOP++ 2.0 [66]. The events were interfaced to PYTHIA 8.230 to model the PS, hadronisation, and UE.

The associated production of a top-quark and a W boson was modelled using the POWHEG BOX v2 generator at NLO in QCD using the five-flavour scheme and the NNPDF3.0_{NLO} set of PDFs. The diagram removal scheme [67] was used to avoid overlap with $t\bar{t}$ production because of interference. Single-top t -channel (s -channel) production was modelled using the POWHEG BOX v2 generator at NLO in QCD using the four-flavour (five-flavour) scheme and the corresponding NNPDF3.0_{NLO} PDF set. The events were interfaced with PYTHIA 8.230 in all cases, except for tW events with large missing transverse momenta, which were interfaced with PYTHIA 8.235.

The production of V +jets was simulated with the SHERPA 2.2.1 generator using NLO-accurate matrix elements for up to two jets, and LO-accurate matrix elements for up to four jets, calculated with the Comix [68] and OPENLOOPS [69, 70] libraries. They were matched with the SHERPA PS [71] using the MEPS@NLO prescription [72–75] using the set of tuned parameters developed by the SHERPA authors. The NNPDF3.0_{NNLO} set of PDFs was used and the samples were normalised to a NNLO prediction [76].

Samples of diboson final states (VV) were simulated with the SHERPA 2.2.1 or 2.2.2 generator, depending on the process, including off-shell effects and Higgs boson contributions, where appropriate. Fully leptonic final states and semileptonic final states, where one boson decays leptonically and the other hadronically, were generated using matrix elements at NLO accuracy in QCD for up to one additional parton and at LO accuracy for up to three additional parton emissions. The matrix element calculations were matched and merged with the SHERPA PS. The NNPDF3.0_{NNLO} set of PDFs was used, along with the internal SHERPA tune.

The production of $t\bar{t}+W$ and $t\bar{t}+Z$ events was modelled using the MADGRAPH5_AMC@NLO 2.3.3 generator at NLO with the NNPDF3.0_{NLO} PDF set. The events were interfaced to PYTHIA 8.210.

The production of $t\bar{t}+H$ events was modelled using the POWHEG BOX v2 generator at NLO with the NNPDF3.0_{NLO} PDF set, interfaced to PYTHIA 8.230.

An overview of the matrix element (ME) generator, PDF, shower generator and UE tune for signal and background samples is given in Table 1.

4 Event reconstruction

Events studied in this analysis are required to have at least one reconstructed pp interaction vertex with at least two associated tracks with transverse momentum $p_T > 0.5$ GeV. The primary vertex is selected as the one with the largest sum of squared transverse momenta of tracks associated with the interaction vertex. In

² The h_{damp} parameter is a resummation damping factor and one of the parameters that controls the matching of POWHEG matrix elements to the PS and thus effectively regulates the high- p_T radiation against which the $t\bar{t}$ system recoils.

Table 1: List of ME generator and the order of the strong coupling constant in the perturbative calculation, PDF, shower generator and tune for the different signal and background processes.

Process	ME generator	ME order	PDF set	PS and hadronisation	UE tune
Scalar LQ	MADGRAPH5_AMC@NLO 2.6.0	NLO	NNPDF3.0NLO	PYTHIA 8.230	A14
Vector LQ	MADGRAPH5_AMC@NLO 2.8.1	LO	NNPDF3.0NLO	PYTHIA 8.244	A14
$t\bar{t}$ /single top	POWHEG BOX v2	NLO	NNPDF3.0NLO	PYTHIA 8.230/8.235	A14
V+jets	SHERPA 2.2.1	MEPS@NLO	NNPDF3.0NNLO	SHERPA	internal
Diboson	SHERPA 2.2.1/2.2.2	MEPS@NLO	NNPDF3.0NNLO	SHERPA	internal
$t\bar{t}+V$	MADGRAPH5_AMC@NLO 2.3.3	NLO	NNPDF3.0NLO	PYTHIA 8.210	A14
$t\bar{t}+H$	POWHEG BOX v2	NLO	NNPDF3.0NLO	PYTHIA 8.230	A14

the analysis, a set of reconstructed objects is used, consisting of electrons, muons, and jets, as well as the missing transverse momentum. When identifying charged leptons, a staggered approach is used, where so-called baseline leptons fulfil less stringent requirements than signal leptons. Events are required to have exactly one signal lepton without any additional baseline leptons.

Electron candidates are reconstructed from energy deposits in the EM calorimeter matched to charged-particle tracks in the inner detector (ID). Requirements of $|d_0|/\sigma_{d_0} < 5$ on the transverse impact parameter d_0 (with uncertainty σ_{d_0}) and $|\Delta z_0 \sin \theta| < 0.5$ mm on the longitudinal track impact parameter z_0 ensure matching between track and vertex. Furthermore, electron candidates are required to lie within a pseudorapidity range of $|\eta| < 2.47$, excluding the EM calorimeter barrel–endcap transition region $1.37 < |\eta| < 1.52$. Baseline electrons must have $p_T > 10$ GeV and fulfil loose identification criteria, using a likelihood-based discriminant that combines information about tracks in the ID and energy deposits in the calorimeter system [77]. In addition, baseline electrons are required to have a hit in the innermost layer of the pixel detector. Isolation requirements in both the calorimeter and the ID are imposed [77]. Electron candidates are rejected if the scalar sum of transverse momenta of tracks within a cone of size $\Delta R = \min(10 \text{ GeV}/p_T, 0.2)$, excluding the electron itself, is larger than 15% of the electron p_T . Similarly, an electron is removed if, after subtracting contributions from pile-up and the electron itself, the transverse energy deposited in the calorimeter within a cone of size $\Delta R = 0.2$ exceeds 20% of the transverse energy of the electron. To suppress backgrounds due to hadrons misidentified as electrons, signal electrons must in addition pass the ‘tight’ identification working point, and have $p_T > 30$ GeV.

Muon candidates are reconstructed from charged-particle tracks in the ID and the MS and from energy deposits in the calorimeters. For the reconstruction of muon candidates, tracks in the ID combined with tracks in the MS are used in the range $|\eta| < 2.5$. In addition, muons in the range $|\eta| < 0.1$ are reconstructed from ID tracks matched to an energy deposit in the calorimeter compatible with a minimally ionising particle. These muon candidates are called calorimeter-tagged (CT). Track-to-vertex matching is ensured by requiring $|d_0|/\sigma_{d_0} < 3$ for the transverse impact parameter and $|\Delta z_0 \sin \theta| < 0.5$ mm for the longitudinal track impact parameter. Baseline muons are required to have $p_T > 10$ GeV and to have compatible individual measurements in the ID and the MS. Signal muons are required to have $p_T > 30$ GeV and CT muons are not accepted [78]. Additionally, signal muons are rejected if the scalar sum of transverse momenta of tracks within a cone of size $\Delta R = \min(10 \text{ GeV}/p_T, 0.3)$ around the muon exceeds 6% of its transverse momentum. In accordance with other searches for pair-produced LQs within ATLAS [32, 33], signal muons above a p_T threshold of 800 GeV must fulfil stricter requirements on the number of hits in the MS to ensure good momentum resolution.

Small-radius (small- R) jet candidates are built from particle-flow objects [79, 80], using the anti- k_t

algorithm [81, 82] with a radius parameter of $R = 0.4$. The particle-flow algorithm combines information about ID tracks and energy deposits in the calorimeters to form the input for jet reconstruction. Jets with $p_T < 25$ GeV or $|\eta| > 2.5$ are rejected. To reduce contributions from pile-up, jet candidates with $|\eta| < 2.4$ and $p_T < 60$ GeV are required to satisfy the ‘tight’ jet vertex tagger criterion [83]. Small- R jets are categorised as b -tagged if they satisfy a requirement on the output of a multivariate algorithm, operating at a tagging efficiency of 77% as determined with simulated $t\bar{t}$ events [84, 85]. The $R = 0.4$ jets are then reclustered with the anti- k_t algorithm with $R = 1.0$ to obtain large- R jets. Additionally, $R = 0.4$ jets are reclustered iteratively with the recursive method described in Ref. [86] to reconstruct hadronically decaying top-quark candidates. For this, the small- R jets are reclustered with an initial radius parameter of $R = 3.0$, which is iteratively reduced to $R(p_T) = 2m_{\text{top}}/p_T$ to match the jet radius to the top candidate’s transverse momentum. Top candidates losing large fractions of their p_T in the shrinking process are discarded. Finally, only the leading- p_T candidate with a mass larger than 150 GeV is kept.

The missing transverse momentum (with magnitude E_T^{miss}) in an event is defined as the negative vectorial sum of the transverse momenta of all calibrated objects [87]. It also includes an additional track-based soft term taking into account energy depositions not associated with any calibrated object.

An overlap removal procedure is applied to avoid ambiguities when reconstructing the objects described above, using the baseline lepton definitions. Electron–muon overlap is handled by removing any calorimeter-tagged muons sharing a track in the ID with an electron, and then removing any electrons sharing an ID track with a remaining muon. Subsequently, overlap between jets and leptons is removed by rejecting any jets within $\Delta R = 0.2$ of an electron and afterwards rejecting any electrons within $\Delta R = 0.4$ of a jet. Similarly, jets are discarded if they have fewer than three associated tracks and are within $\Delta R = 0.2$ of a muon candidate. Otherwise, the muon is rejected if it lies within $\Delta R = \min(0.4, 0.04 + 10 \text{ GeV}/p_T(\mu))$ of a jet.

5 Event selection and categorisation

Any event considered in this analysis must pass an E_T^{miss} trigger [88]. Because the trigger thresholds varied, a requirement of $E_T^{\text{miss}} > 250$ GeV is imposed in the offline event selection to ensure full efficiency of all the triggers across the different data-taking periods. Events are required to contain exactly one signal lepton. Additionally, a veto is applied on further baseline leptons. Since the final states of interest contain one hadronically decaying top-quark and one additional jet, only events with at least four jets are selected. Only one of those jets needs to be b -tagged to preserve high efficiency for the signal. To suppress contributions from fake E_T^{miss} caused by mismeasurements of jets or leptons, events with $m_T(\ell, E_T^{\text{miss}}) = \sqrt{2p_T(\ell)E_T^{\text{miss}}(1 - \cos \Delta\phi(p_T(\ell), E_T^{\text{miss}}))} < 30$ GeV or $\Delta\phi(E_T^{\text{miss}}, j_{1,2}) < 0.4$, where $j_{1,2}$ indicates the highest- p_T and the second-highest- p_T small- R jet, respectively, are rejected.

As the $t\bar{t}$ background is known not to be modelled accurately at high transverse momenta [89, 90], reweighting factors are derived in bins of the jet multiplicity as a function of m_{eff} , which is defined as the scalar sum of the transverse momenta of all reconstructed objects and the E_T^{miss} . This procedure is referred to as ‘top reweighting’ in the following. The reweighting factors are determined for the sum of the $t\bar{t}$ and single-top backgrounds and are parameterised with a linear function, separately in each of the four jet multiplicity bins (4, 5, 6, ≥ 7). For this, a dedicated top reweighting region is defined with $am_{T2} < 200$ GeV, where the asymmetric transverse mass, am_{T2} , is a variant of m_{T2} [91] and allows the reconstruction of dileptonic $t\bar{t}$ events in which only one lepton is reconstructed [92, 93]. The reweighting

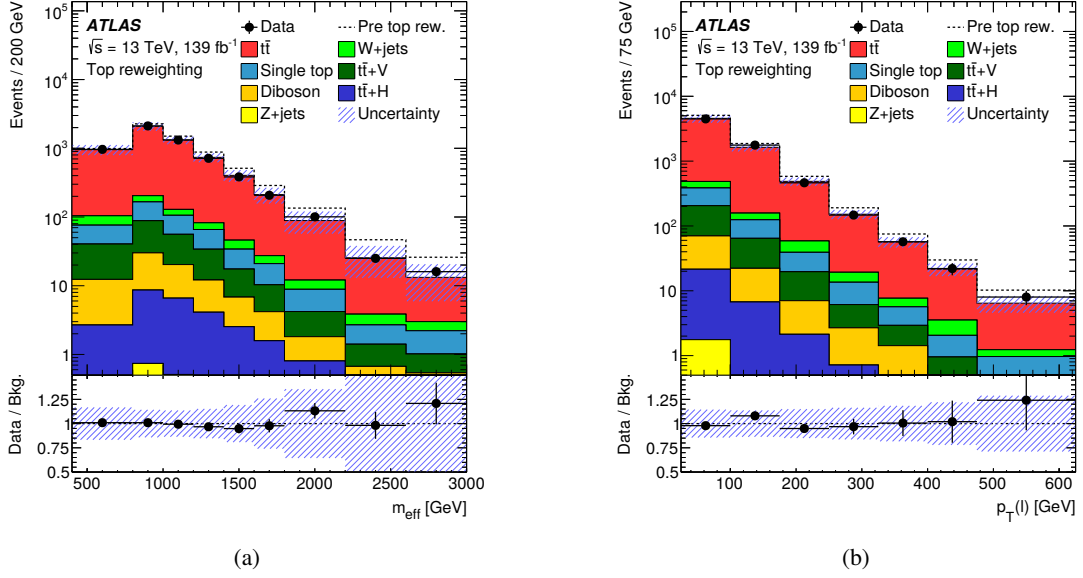


Figure 2: Distributions of (a) m_{eff} and (b) $p_T(\ell)$ in the top reweighting region after applying the top reweighting. The hatched bands include statistical and systematic uncertainties. The total background expectation before applying the top reweighting is shown as a dashed line. The ratios of the observed and expected numbers of background events are shown in the bottom panels. The last bin contains the overflow.

factor is then applied to single-top and $t\bar{t}$ events in each of the training and control regions defined in the following. Figure 2 shows the m_{eff} and lepton- p_T distributions in the top reweighting region after applying the reweighting procedure, in addition to the total background expectation before reweighting. The modelling of kinematic variables is improved by the correction.

Control regions (CRs) enriched in the various backgrounds and with negligible signal contamination are defined. They are orthogonal to the top reweighting region by requiring $am_{T2} > 200$ GeV and are orthogonal to each other. The W +jets CR uses events in a window around the Jacobian peak, i.e. $50 \text{ GeV} \leq m_T(\ell, E_T^{\text{miss}}) < 120$ GeV, with a b -jet multiplicity of $n_b = 1$ and no hadronically decaying top-quark candidate. To increase the purity of selected W +jets events, only events with a positively charged lepton are considered, because the cross-section for W^+ production is larger than that for W^- production in pp collisions. For the single-top CR a requirement of $m_T(\ell, E_T^{\text{miss}}) < 120$ GeV is imposed. In order to reduce contributions from W +jets production, events must have exactly two b -tagged jets, with an angular separation $\Delta R(b_1, b_2) > 1.2$. Events containing a large- R jet are vetoed. Distributions of m_{eff} in the W +jets CR and the single-top CR are shown in Figure 3.

For the training of the NNs, a training region is defined so as to be orthogonal to the top reweighting region and both control regions by requiring $am_{T2} > 200$ GeV and $m_T(\ell, E_T^{\text{miss}}) \geq 120$ GeV. An overview of the different selection requirements for the training and control regions is given in Table 2. The product of signal acceptance and efficiency in the training region is similar for signal hypotheses with couplings to electrons or muons. For $\mathcal{B} = 0.5$, it amounts to around 17% for up-type scalar LQs and to around 14% for down-type scalar LQs at $m_{\text{LQ}} = 1.4$ TeV. For vector LQs, it reaches 20% at the same mass for both the Yang–Mills coupling and the minimal coupling scenario.

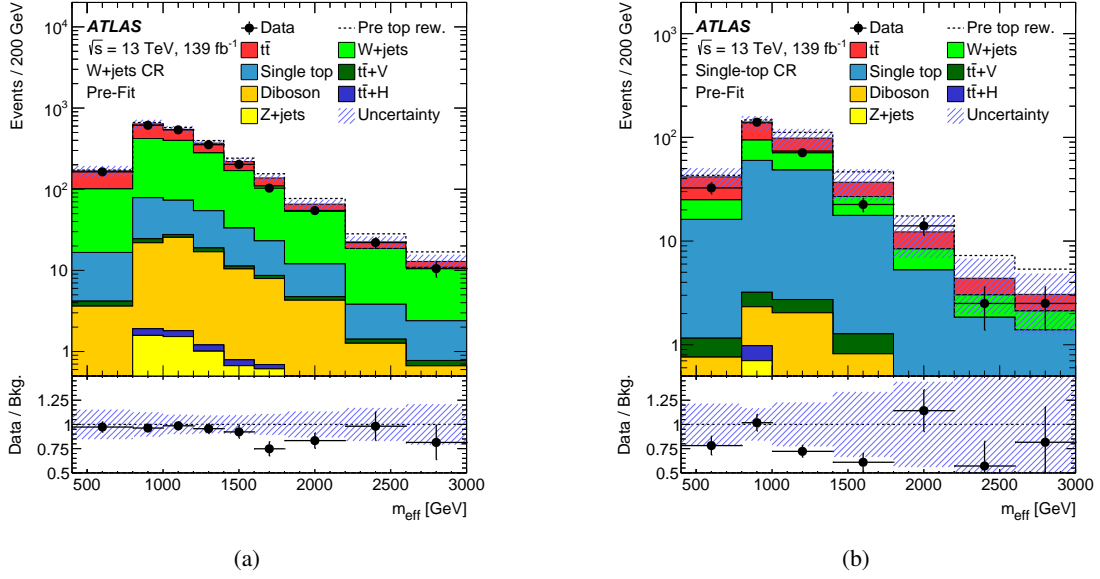


Figure 3: Distributions of m_{eff} in (a) the W +jets CR and (b) the single-top CR after applying the top reweighting, before the fit to data in CRs and SR. The hatched bands include statistical and systematic uncertainties. The total background expectation before applying the top reweighting is shown as a dashed line. The ratios of the observed and expected numbers of background events are shown in the bottom panels. The last bin contains the overflow.

Table 2: Overview of event selections applied in the different regions of the analysis.

Preselection				
$E_{\text{T}}^{\text{miss}}$ triggers				
exactly one signal lepton				
veto on additional baseline leptons				
$E_{\text{T}}^{\text{miss}} > 250$ GeV				
≥ 4 small- R jets				
$m_{\text{T}}(\ell, E_{\text{T}}^{\text{miss}}) > 30$ GeV				
$\Delta\phi(E_{\text{T}}^{\text{miss}}, j_{1,2}) > 0.4$				
Top reweighting region	W +jets CR	Single-top CR	Training region	
$n_b \geq 1$	$n_b = 1$	$n_b = 2$	$n_b \geq 1$	
$m_{\text{T}}(\ell, E_{\text{T}}^{\text{miss}}) \geq 120$ GeV	$50 \text{ GeV} \leq m_{\text{T}}(\ell, E_{\text{T}}^{\text{miss}}) < 120$ GeV	$m_{\text{T}}(\ell, E_{\text{T}}^{\text{miss}}) < 120$ GeV	$m_{\text{T}}(\ell, E_{\text{T}}^{\text{miss}}) \geq 120$ GeV	
$am_{\text{T}2} < 200$ GeV	$am_{\text{T}2} > 200$ GeV	$am_{\text{T}2} > 200$ GeV	$am_{\text{T}2} > 200$ GeV	
-	t_{had} candidate veto	large- R jet veto	-	
-	lepton charge = $+1e$	-	-	
-	-	$\Delta R(b_1, b_2) > 1.2$	-	

6 Neural network training

Simulated signal and background events in the training region are used to train several NNs for the various signal hypotheses. The NNs are implemented using the NeuroBayes package [94, 95] which combines a three-layer feed-forward NN with a complex and robust preprocessing of the input variables prior to their presentation to the NN. The purpose of the preprocessing is to facilitate optimal network training by ordering the input variables according to their ability to discriminate between signal and background, taking correlations into account, and removing all but the most powerful ones.

NeuroBayes uses Bayesian regularisation techniques for the training process to improve the generalisation performance and to avoid overtraining. In general, the network infrastructure consists of one input node for each input variable plus one bias node, an arbitrary, user-defined number of hidden nodes, and one output node which gives a continuous NN output score (NN_{out}) in the interval $(0, +1)$, where large values indicate signal-like events and small values background-like events. For the NNs of this analysis, 15 nodes are used in the hidden layer and the ratio of signal to background events in the training is 1:1. The different background processes are weighted according to their expected number of events. Only $t\bar{t}$, W +jets, single-top-quark, and $t\bar{t}+V$ events are used as background processes in the training. As a check for potential overtraining, only 80% of the simulated events serve as input to the training, while the remaining 20% are used as a test sample. No signs of overtraining are observed. After the training step, samples of simulated signal and background events, as well as the observed events, are processed by the NNs in order to get an NN_{out} value for each event. For each NN, the training region is divided into a low- NN_{out} control region with $NN_{\text{out}} < 0.5$, enriched mainly in $t\bar{t}$ events, and the signal region above 0.5.

The input variables are chosen because of their ability to discriminate between signal and background. In total, 15 input variables are provided for the training, including the lepton flavour in order to distinguish between electrons and muons. This is because a final state with one lepton flavour has some sensitivity to a LQ model with the other flavour if the lepton stems from a top-quark decay, i.e. mainly in the low \mathcal{B} region. Table 3 lists the input variables in order of decreasing ability to discriminate between signal and background. The order is not absolute, as there is some dependence on the signal model and \mathcal{B} , e.g. the lepton flavour cannot discriminate at all in the region of low \mathcal{B} , but is important otherwise. The modelling of the input variables in the training region is good in general, as can be seen for the most important ones in Figure 4. Among the least well modelled of all input variables is $m_{\text{inv}}(b_1, \ell)$ shown in Figure 4(c). This is due to the interference between single-top and $t\bar{t}$ production, which is difficult to describe in MC simulations [96].

Figure 4 also displays three up-type signal hypotheses at a mass of 1.3 TeV. It can be seen that the signal shape depends not only on the value of \mathcal{B} but also on the spin of the LQ. The signal shape differences due to spin correlations are sizeable for low values of \mathcal{B} at small values of lepton p_T , where the lepton usually originates from a top-quark decay. The lepton- p_T distribution in the vector LQ model is found to be similar in shape to the background in contrast to the scalar case as can be seen Figure 4(b). Therefore, separate NNs are trained for scalar and vector LQs as well as for various values of \mathcal{B} . A total of four NNs per lepton flavour at $\mathcal{B} = 0.0, 0.25, 0.5$, and 0.9 are used for up-type scalar and vector LQs. Since kinematic differences between the Yang–Mills coupling and the minimal coupling are negligible except for very low masses, the NNs for vector LQs are only trained on samples with the former coupling and then applied to the latter as well. In the case of down-type scalar LQs, only one NN is trained for LQs decaying into muons and another is trained for LQs decaying into electrons. For both trainings, a branching ratio of 0.5 is assumed, since only events with one LQ decaying into a charged lepton and the other decaying into a neutrino contribute significantly to the phase space under consideration. For scalar LQs,

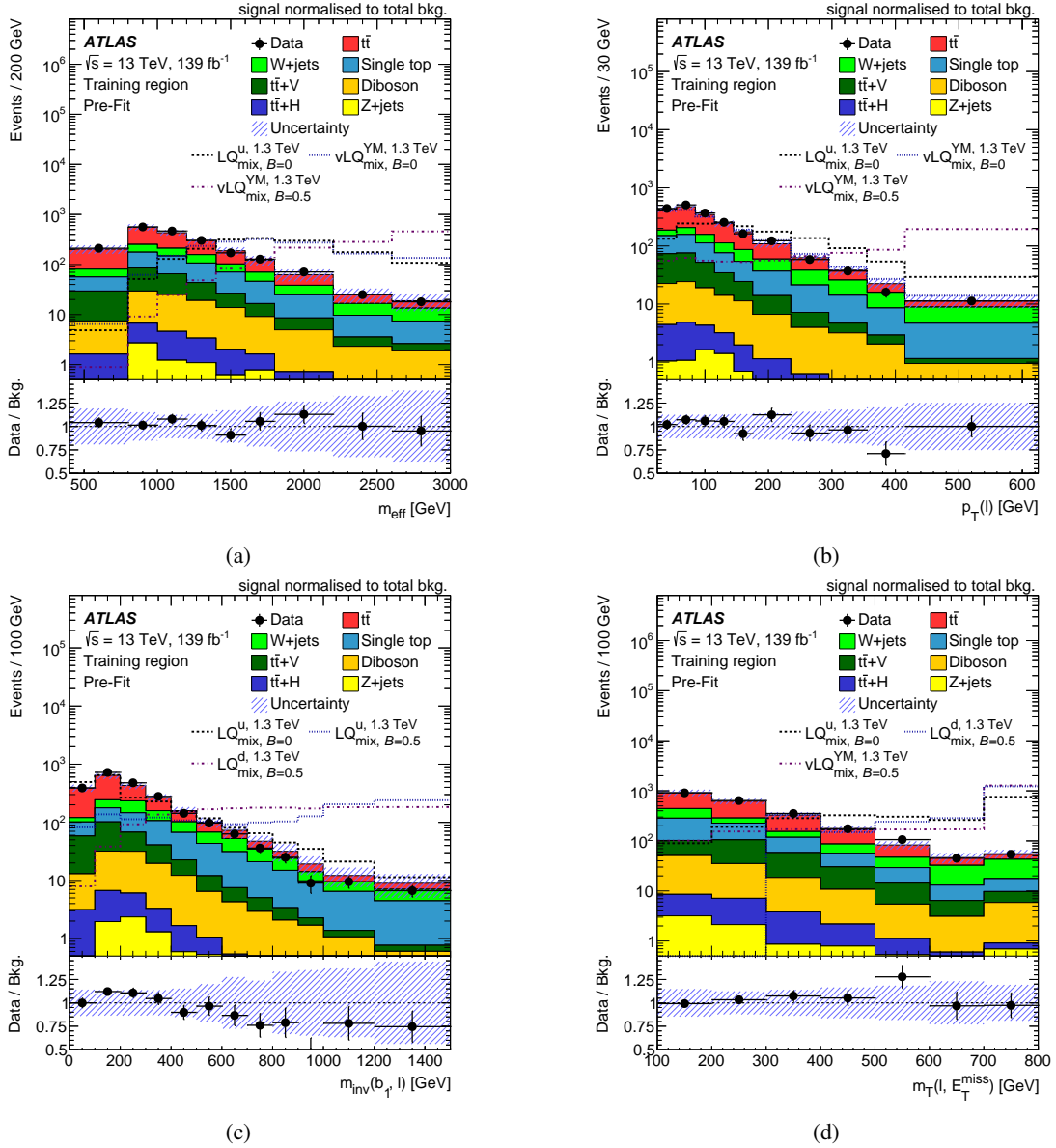


Figure 4: Distributions of (a) m_{eff} , (b) $p_T(\ell)$, (c) $m_{\text{inv}}(b_1, \ell)$, and (d) $m_T(\ell, E_T^{\text{miss}})$ in the training region after applying the top reweighting, before the fit to data in CRs and SR. The hatched bands include statistical and systematic uncertainties. Signal distributions normalised to the total background expectation are overlaid for up-type scalar LQs with $\mathcal{B} = 0.0$ and vector LQs with $\mathcal{B} = 0.0$ and 0.5 , each with $m_{LQ} = 1.3$ TeV. The ratios of the observed and expected numbers of background events are shown in the bottom panels. The last bin contains the overflow.

Table 3: Input variables for the NN training, approximately sorted in descending ability to discriminate between signal and background. The order is not absolute as there is some dependence on the signal model and \mathcal{B} .

Variable	Description
$m_T(\ell, E_T^{\text{miss}})$	transverse mass of lepton and E_T^{miss}
m_{eff}	scalar sum of the transverse momenta of leptons, jets, and E_T^{miss}
Lepton flavour	flavour of the signal lepton
$p_T(\ell)$	transverse momentum of the lepton
$m_{\text{inv}}(b_1, \ell)$	invariant mass of the leading- p_T b -jet and the lepton
n_{large}	reclustered large- R jet multiplicity
am_{T2}	asymmetric transverse mass
E_T^{miss} significance	measure for assessing the compatibility of the observed E_T^{miss} with zero, taking resolutions into account
$m_T(b_1, E_T^{\text{miss}})$	transverse mass of leading- p_T b -jet and E_T^{miss}
$p_T(t_{\text{had}})$	transverse momentum of t_{had}
$\Delta\phi(E_T^{\text{miss}}, b_2)$	azimuthal angle separation between E_T^{miss} and subleading- p_T b -jet
$m_{\text{inv}}(b_2, \ell)$	invariant mass of subleading- p_T b -jet and lepton
$\Delta\phi(E_T^{\text{miss}}, b_1)$	azimuthal angle separation between E_T^{miss} and leading- p_T b -jet
$\Delta\phi(t_{\text{had}}, \ell)$	azimuthal angle separation between t_{had} and lepton
$p_T(b_1)$	transverse momentum of leading- p_T b -jet

signal samples produced with $m_{LQ} = 500$ GeV, 900 GeV, and 1300 GeV are combined in each training, as separate trainings for each signal mass did not yield a significant improvement for masses above about 600 GeV. For vector LQs, additional signal samples with $m_{LQ} = 1700$ GeV are used to take advantage of their higher production cross-sections and therefore higher expected mass limits.

7 Systematic uncertainties

The largest systematic uncertainties considered in the analysis are related to the modelling of the background processes. For $t\bar{t}$ production, the uncertainty due to the method used to match the matrix element to the parton shower is assessed by comparing a sample produced by MADGRAPH5_AMC@NLO with the nominal sample from POWHEG BOX, using the same parton shower. Conversely, an estimate of the uncertainties related to the underlying event, parton shower, and hadronisation is obtained by comparing a sample showered by HERWIG 7 [97] with the nominal sample showered by PYTHIA, using the same ME generator for both. The effects of uncertainties in the renormalisation and factorisation scales are estimated by independently varying the scales by a factor of two. The impact of initial-state radiation (ISR) is estimated by varying α_s in the A14 tune. Similarly, the uncertainty related to final-state radiation (FSR) is assessed by varying the renormalisation scale for final-state parton-shower emissions by a factor of two. Additionally, an uncertainty related to the choice of value for the POWHEG BOX-specific h_{damp} parameter is evaluated by using a varied value of $h_{\text{damp}} = 3.0 m_t$. PDF uncertainties are obtained from the PDF4LHC15 PDF set [98].

For single top-quark production, uncertainties in ME-to-PS matching, the choice of parton shower, renormalisation and factorisation scales, ISR, FSR, and PDF are evaluated using the same procedures as for $t\bar{t}$ production. Large uncertainties arise due to interference effects between $t\bar{t}$ and tW production. They

are estimated by comparing the nominal sample based on the diagram removal scheme with a sample using the diagram subtraction scheme [67, 99].

In the top reweighting procedure, the parameters of the linear fit are varied within their 2σ uncertainty to account for potential non-linearities in addition to the statistical uncertainty, treating the normalisation and the shape component in each of the four jet multiplicity bins independently. Compared to the 1σ variation, this choice has a negligible impact on the results.

For W +jets, Z +jets, diboson, $t\bar{t}+V$, and $t\bar{t}+H$ processes, renormalisation and factorisation scale variations are considered, following the same procedures as for $t\bar{t}$. In addition, an uncertainty of 50% is assigned to the heavy-flavour component of the W +jets background to cover differences in flavour composition between control and signal regions seen in MC studies.

Theoretical systematic uncertainties also include cross-section uncertainties for the background processes for which no normalisation parameters enter the profile-likelihood fit. For diboson and Z +jets production, this uncertainty is taken to be 6% [100] and 5% [101], respectively. For $t\bar{t}+H$ production, it amounts to 11% [102] and for $t\bar{t}+Z$ production to 15% [102]. For $t\bar{t}+W$ production, the cross-section uncertainty is taken to be 50% to account for potential differences between predicted and measured values as reported in Ref. [103].

Systematic uncertainties in the signal prediction arise from acceptance effects due to renormalisation and factorisation scale, ISR/FSR, and PDF and α_s variations. They were found to not exceed 5% in total across the whole mass range, and this is therefore taken as a conservative estimate.

Additionally, detector-related uncertainties are considered, the dominant ones being the small- R jet energy scale and resolution uncertainties [80]. Furthermore, systematic uncertainties related to the jet mass scale and resolution, the lepton identification, isolation, and reconstruction efficiencies as well as the lepton energy scale and resolution [77, 78], the b -tagging efficiencies [84], and the E_T^{miss} reconstruction [104] are taken into account. Minor contributions to the total systematic uncertainty also come from the uncertainty of 1.7% in the integrated luminosity [105], obtained using the LUCID-2 detector [106] for the primary luminosity measurements, and from an uncertainty related to pile-up reweighting.

8 Statistical interpretation

The binned distributions of the NN output are used to test for the presence of a signal. Simultaneous binned profile-likelihood fits are performed for hypothesis testing, following a modified frequentist method implemented in RooStats [107] and using the NN_{out} distribution in the signal region and the overall number of events in the low- NN_{out} , W +jets, and single-top control regions. Systematic uncertainties affecting signal and background expectations are accounted for by including them in the fit in the form of nuisance parameters. For uncertainties in the modelling of background processes for which the normalisation is determined in the likelihood fit, only shape effects and acceptance differences between the CRs and the SR are considered, in order to avoid double-counting of normalisation uncertainties. This procedure is also used for pre-fit uncertainty bands in order to have an equivalent treatment of systematic uncertainties. A smoothing algorithm is applied to certain systematic variations in the signal region in order to reduce statistical fluctuations between bins. To simplify the fitting procedure, for each region and each process a nuisance parameter is only considered if the overall effect on the normalisation of the process is larger than 1%. In the case of the signal region, which has multiple bins, nuisance parameters are also considered if their effect in any bin within the signal region is above 1%.

The binned likelihood function $\mathcal{L}(\mu, \theta)$ is constructed as the product of Poisson probability terms over all bins considered in the analysis. It depends on the signal strength parameter μ , a multiplicative factor applied to the theoretical signal production cross-section, and θ , a set of nuisance parameters, implemented in the likelihood function as Gaussian or log-normal priors. The expected number of events in a bin depends on μ and θ . The nuisance parameters θ adjust the expectations for signal and background according to the corresponding systematic uncertainties, and their fitted values correspond to the amounts that best fit the data.

The test statistic q_μ is defined as the profile likelihood ratio

$$q_\mu = -2 \ln \frac{\mathcal{L}(\mu, \hat{\theta})}{\mathcal{L}(\hat{\mu}, \hat{\theta})},$$

where $\hat{\mu}$ and $\hat{\theta}$ are the values of the parameters that maximise the likelihood function (with the constraints $0 \leq \hat{\mu} \leq \mu$), and $\hat{\theta}$ are the values of the nuisance parameters that maximise the likelihood function for a given value of μ . This test statistic is used to determine whether the observed data are compatible with the background-only hypothesis, i.e. with $\mu = 0$. Furthermore, by using the CL_s method [108], upper limits on the signal production cross-section are derived for each of the signal scenarios considered in this analysis. For a given signal scenario, values of the production cross-section (parameterised by μ) yielding $\text{CL}_s < 0.05$, where CL_s is computed using the asymptotic approximation [109], are excluded at $\geq 95\%$ confidence level (CL).

9 Results

For each NN training, a separate fit to the NN_{out} distribution in the signal region and the overall number of events in the low- NN_{out} , W +jets, and single-top control regions is performed, with free normalisation parameters for the $t\bar{t}$, single-top, and W +jets background processes. The normalisation parameters obtained from fits to data using the background-only hypothesis are consistent across all trainings. They are always applied in the following and vary between 1.09 ± 0.22 and 1.29 ± 0.23 for $t\bar{t}$, between 0.84 ± 0.12 and 0.93 ± 0.12 for W +jets, and between 0.46 ± 0.27 and 0.54 ± 0.26 for single top. The normalisation parameter for the single-top process reduces the event yield by approximately a factor of two; however, the expected yield from the alternative scheme to model the interference between the $t\bar{t}$ and tW processes leads to an even smaller yield. Observed and expected event yields after the background-only fit are listed in Table 4 for one NN training.

The NN_{out} distributions after the background-only fit are validated with data–MC comparisons in the control regions, as shown in Figure 5 for one particular NN training. In general, good agreement is found for all trainings in all control regions, although the single-top CR is typically more problematic due to the interference effects mentioned above [96]. NPs corresponding to the systematic uncertainties covering the observed differences between data and MC simulation are not constrained significantly because only the overall number of events in each CR enters the fit. The systematic uncertainties are therefore fully propagated to the SR.

A comparison between data and background expectation in the signal region is shown in Figure 6 after the background-only fit for three different NN trainings. Good agreement is found for all trainings. The largest discrepancies at high values of NN_{out} are observed for the LQ_{mix}^u model with $\mathcal{B} = 0.0$, i.e. for the decay into top-quarks and neutrinos as shown in Figure 6(c).

Table 4: Observed and expected event yields in the control and signal regions for a training for $\nu\text{LQ}_{\text{mix}}^{\text{YM}} \rightarrow b\mu/t\nu$ and $\mathcal{B} = 0.5$ after the background-only fit. The uncertainties in the background predictions include both the statistical and systematic components. For comparison, expected event yields are shown for a $\nu\text{LQ}_{\text{mix}}^{\text{YM}}$ signal at a mass point of 1700 GeV and $\mathcal{B} = 0.5$ including its pre-fit uncertainties.

	W+jets CR	Single-top CR	Low- NN_{out} CR	SR
$t\bar{t}$	860 ± 140	186 ± 35	1370 ± 150	53 ± 10
Single top	103 ± 87	131 ± 47	200 ± 110	36 ± 14
W+jets	1240 ± 130	101 ± 28	265 ± 55	32.4 ± 6.9
$t\bar{t}+V$	11.0 ± 1.8	4.47 ± 0.79	180 ± 28	16.7 ± 2.6
Diboson	94.3 ± 9.8	7.6 ± 1.9	94 ± 11	11.1 ± 1.2
$t\bar{t}+H$	1.27 ± 0.16	1.00 ± 0.12	14.4 ± 1.7	1.34 ± 0.18
Z+jets	6.46 ± 0.32	2.18 ± 0.11	7.20 ± 0.36	1.315 ± 0.072
Total background	2308 ± 48	433 ± 21	2126 ± 46	152 ± 13
Observed events	2310	430	2124	157
$\nu\text{LQ}_{\text{mix}}^{\text{YM}}$ (1.7 TeV, $\mathcal{B} = 0.5$)	0.109 ± 0.022	0.097 ± 0.016	1.57 ± 0.10	38.9 ± 2.6

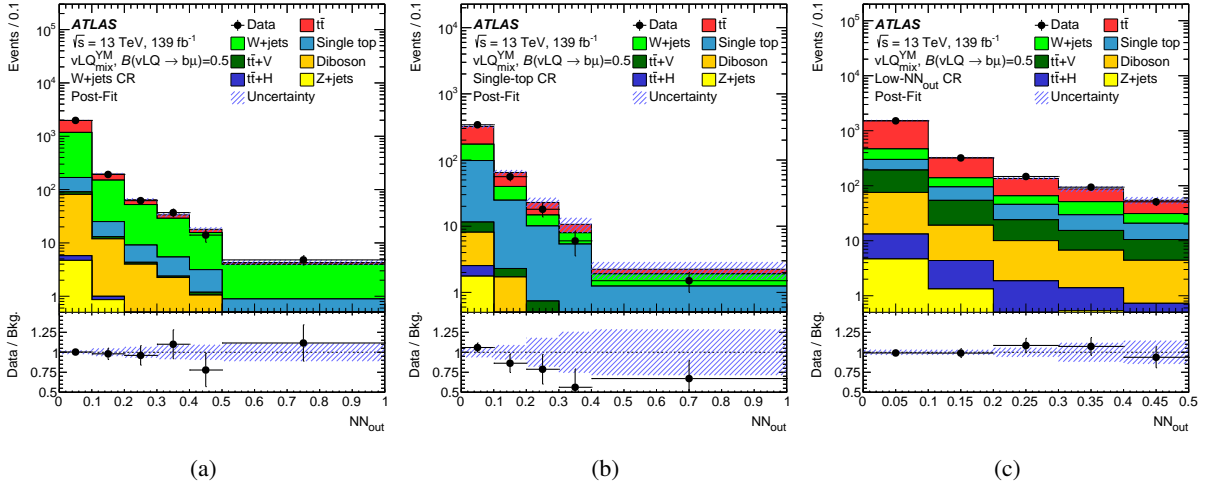


Figure 5: Data and background expectation in (a) the W+jets CR, (b) the single-top CR, and (c) the low- NN_{out} CR after the simultaneous background-only fit for a training with $\nu\text{LQ}_{\text{mix}}^{\text{YM}} \rightarrow b\mu/t\nu$ and $\mathcal{B} = 0.5$. The hatched band indicates the total post-fit uncertainty. The ratios of data to background expectation are shown in the bottom panels.

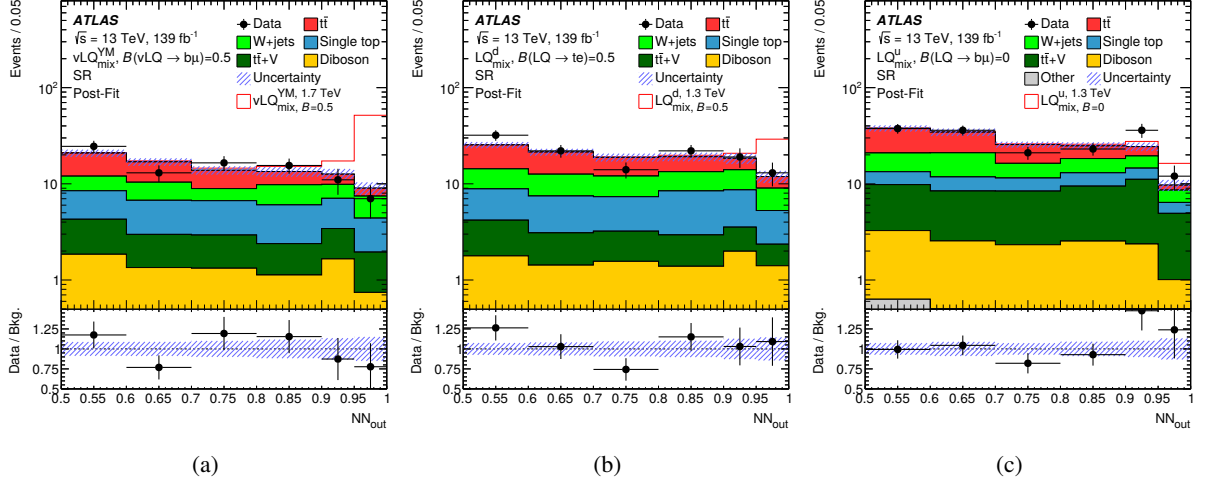


Figure 6: Data and background expectation in the signal region after the simultaneous background-only fit to data for (a) a training with $vLQ_{\text{mix}}^M \rightarrow b\mu/t\nu$ and $\mathcal{B} = 0.5$, (b) a training with $LQ_{\text{mix}}^d \rightarrow te/b\nu$ with $\mathcal{B} = 0.5$, and (c) a training with $LQ_{\text{mix}}^u \rightarrow t\nu$, i.e. $\mathcal{B} = 0.0$. Minor background contributions from $t\bar{t}+H$ and Z +jets are combined into ‘other’. Expected pre-fit signal distributions with \mathcal{B} corresponding to the respective training are added on top of the background expectation, using a mass of 1700 GeV for vector LQs and 1300 GeV for scalar LQs. The hatched band indicates the total post-fit uncertainty. The ratios of data to background expectation are shown in the bottom panels.

No significant deviations of the data from the expected SM background are observed. Upper 95% CL limits on the cross-sections of pair-produced LQs can be calculated in simultaneous signal-plus-background fits to the CRs and the SR, in which the background normalisations and possible signal contributions are determined. The largest uncertainty in each of the resulting signal strengths is statistical in nature. For the three signal hypotheses shown in Figure 6, the statistical uncertainty exceeds 85% of the total uncertainty for the two scalar LQ models at $m_{LQ} = 1.3$ TeV and rises to nearly 100% for the vector LQ case at $m_{LQ} = 1.7$ TeV. The resulting limits on the cross-section for the four scalar LQ models are shown in Figure 7 as a function of the LQ mass for a fixed $\mathcal{B} = 0.5$. Corresponding limits for the four vector LQ models are shown in Figure 8.

These cross-section limits are compared with the theoretical cross-section predictions, shown in blue, resulting in lower limits on the signal mass for $\mathcal{B} = 0.5$. The uncertainty band around the theory prediction includes PDF, α_s , and renormalisation and factorisation scale uncertainties. The expected and observed limits for $\mathcal{B} = 0.5$ are summarised in Table 5 for the eight LQ models considered in this analysis. The total impact of systematic uncertainties on the cross-section limits reaches 15% for LQ masses above 1 TeV, corresponding to 20 GeV in the expected mass limit.

Limits on LQ pair-production are also evaluated across a wide range of values for the branching ratio of LQs into charged leptons. For that, the statistical interpretation is performed in steps of 0.05 in \mathcal{B} between 0.0 and 0.95 for up-type scalar and vector LQs and between 0.05 and 0.95 for down-type scalar LQs. For up-type LQs, for which NNs have been trained at four different values of \mathcal{B} , the NN resulting in the best expected cross-section limit is chosen at each step. The analysis is not sensitive to final states with zero or two leptons; therefore, $\mathcal{B} = 1.0$ is omitted for all LQs and so is $\mathcal{B} = 0.0$ for down-type LQs. The cross-section upper limits and the mass exclusion curves across the \mathcal{B} plane are shown in Figure 9 for scalar LQs and in Figure 10 for vector LQs.

Expected and observed limits on the leptoquark mass as a function of \mathcal{B} agree well everywhere, except for

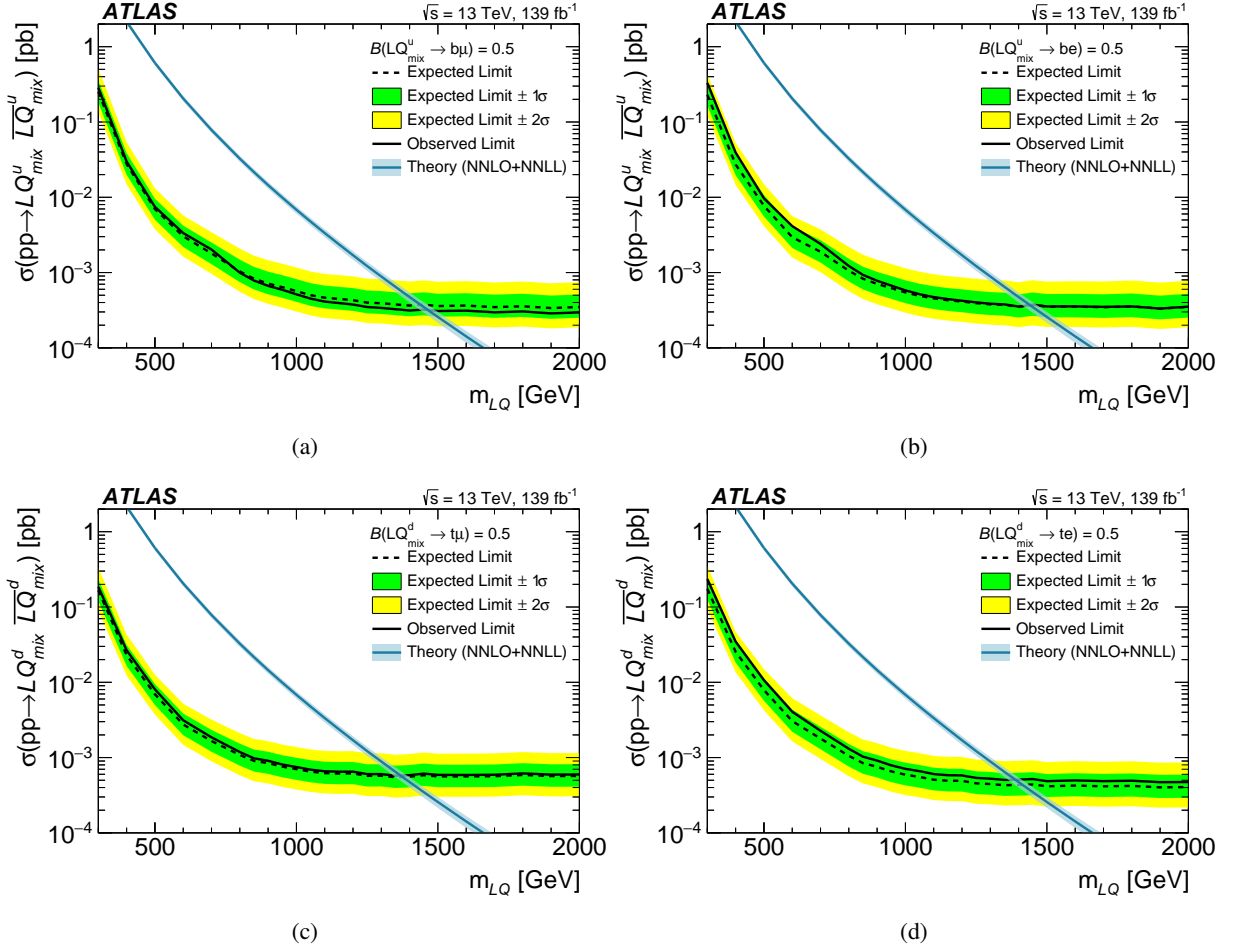


Figure 7: Expected (dashed black) and observed (solid black) 95% CL upper limits on the cross-section of pair-produced scalar LQs, assuming $\mathcal{B} = 0.5$. The green (yellow) band shows the $\pm 1\sigma$ ($\pm 2\sigma$) uncertainty region around the expected limit. The theoretical prediction and its $\pm 1\sigma$ uncertainty band are shown in blue. Limits are presented for (a) up-type scalar LQs decaying into muons, (b) up-type scalar LQs decaying into electrons, (c) down-type scalar LQs decaying into muons, and (d) down-type scalar LQs decaying into electrons.

Table 5: Expected and observed 95% CL lower limits on the LQ mass at $\mathcal{B} = 0.5$ for the eight signal hypotheses considered in this analysis.

	Exp. limit [GeV]	Obs. limit [GeV]
$LQ_{\text{mix}}^u \rightarrow tv/b\mu$	1440^{+60}_{-60}	1460
$LQ_{\text{mix}}^u \rightarrow tv/be$	1440^{+60}_{-60}	1440
$LQ_{\text{mix}}^d \rightarrow t\mu/b\nu$	1380^{+50}_{-60}	1370
$LQ_{\text{mix}}^d \rightarrow te/b\nu$	1410^{+60}_{-60}	1390
$\nu LQ_{\text{mix}}^{\text{YM}} \rightarrow tv/b\mu$	1930^{+50}_{-60}	1980
$\nu LQ_{\text{mix}}^{\text{YM}} \rightarrow tv/be$	1930^{+50}_{-70}	1900
$\nu LQ_{\text{mix}}^{\text{min}} \rightarrow tv/b\mu$	1660^{+50}_{-50}	1710
$\nu LQ_{\text{mix}}^{\text{min}} \rightarrow tv/be$	1650^{+50}_{-60}	1620

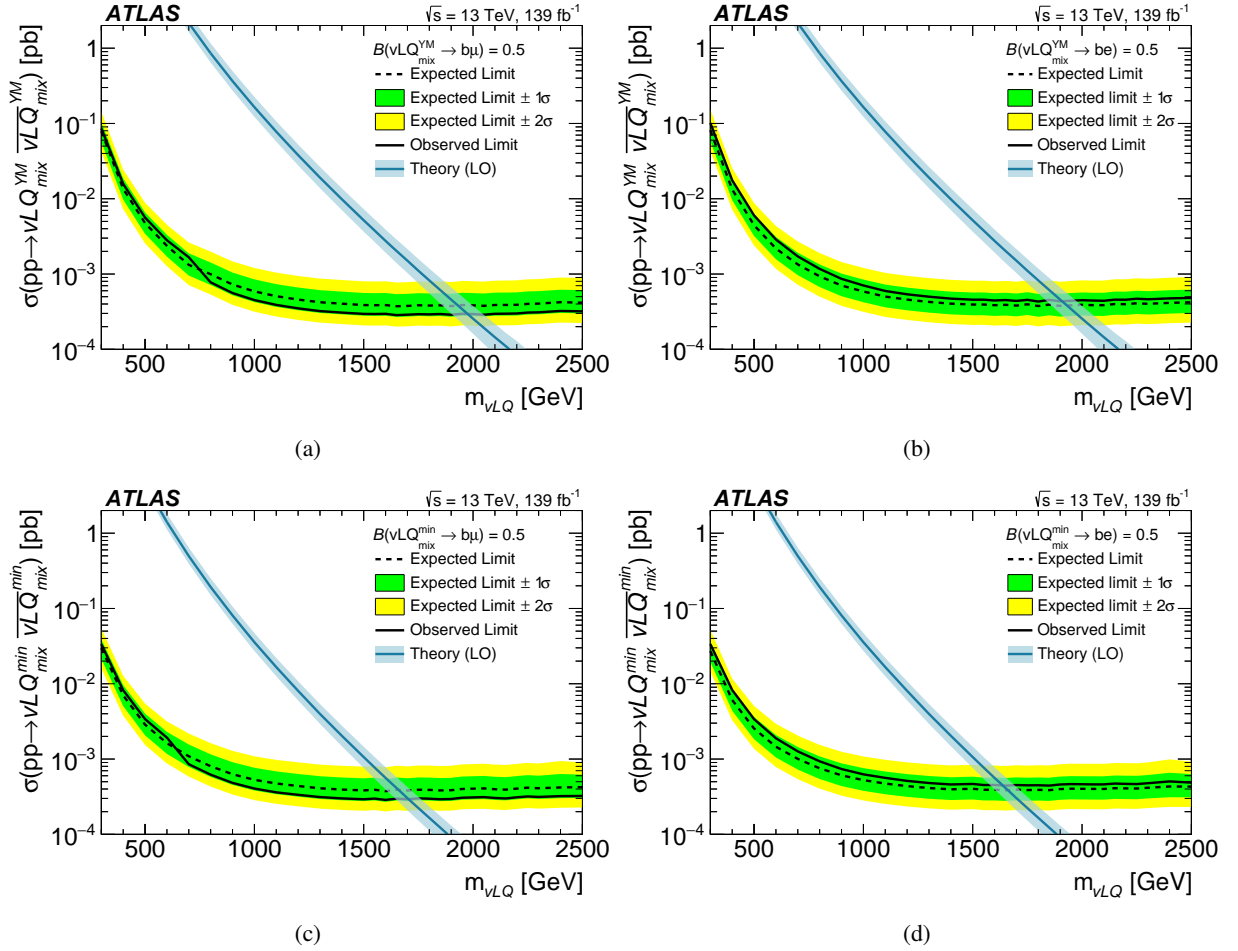


Figure 8: Expected (dashed black) and observed (solid black) 95% CL upper limits on the cross-section of pair-produced vector LQs, assuming $\mathcal{B} = 0.5$. The green (yellow) band shows the $\pm 1\sigma$ ($\pm 2\sigma$) uncertainty region around the expected limit. The theoretical prediction and its $\pm 1\sigma$ uncertainty band are shown in blue. Limits are presented for (a) vector LQs in the Yang–Mills coupling scenario decaying into muons, (b) vector LQs in the Yang–Mills coupling scenario decaying into electrons, (c) vector LQs in the minimal coupling scenario decaying into muons, and (d) vector LQs in the minimal coupling scenario decaying into electrons.

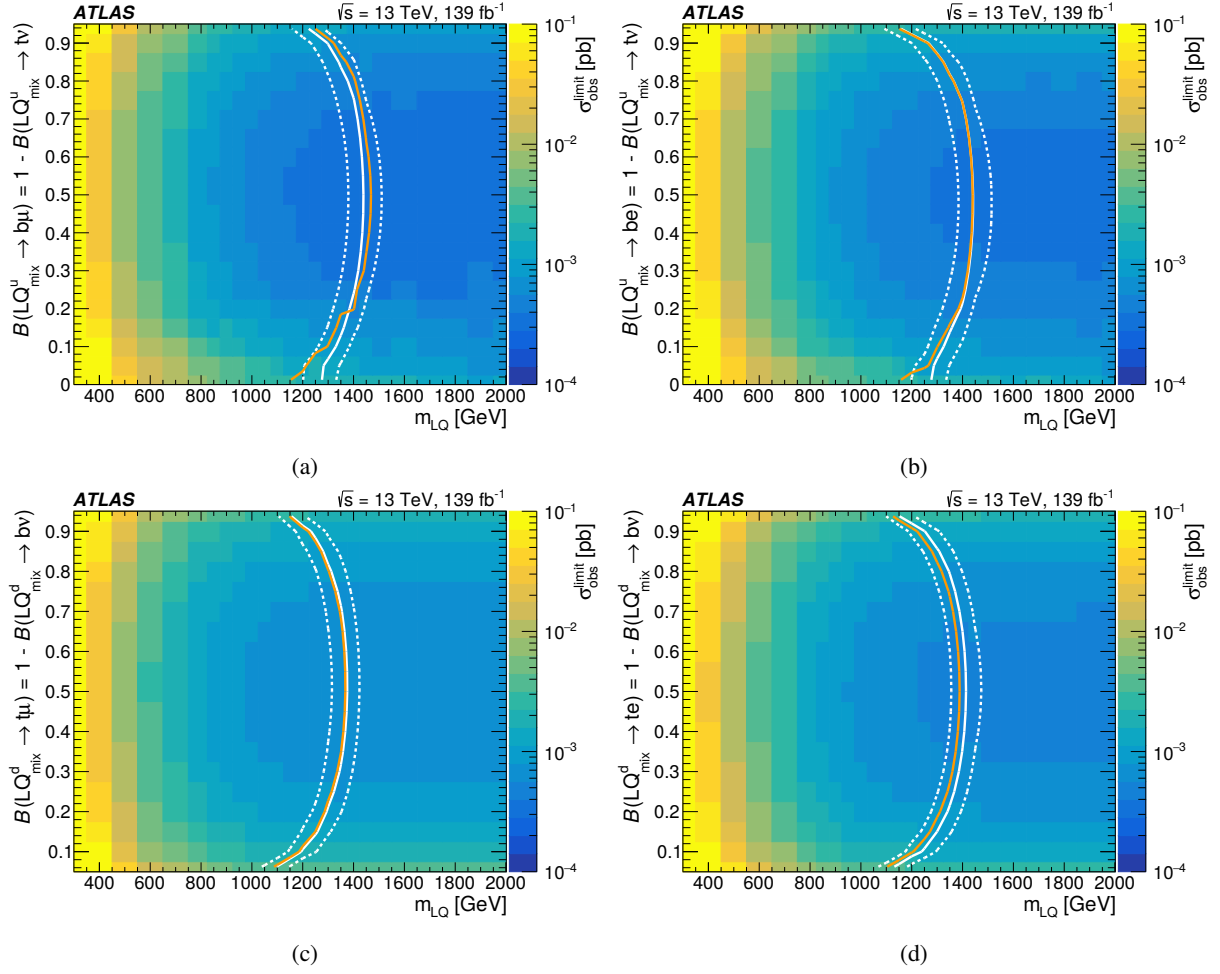


Figure 9: Expected (solid white, $\pm 1\sigma$ ranges dashed) and observed (solid red) exclusion limits on the leptoquark mass as a function of the branching ratio into charged leptons at 95% CL. The observed upper limit on the signal cross-section in each bin is shown on the z-axis. Limits are presented for (a) up-type scalar LQs decaying into muons, (b) up-type scalar LQs decaying into electrons, (c) down-type scalar LQs decaying into muons, and (d) down-type scalar LQs decaying into electrons. For up-type LQs the range in \mathcal{B} is 0–0.95, for down-type it is 0.05–0.95.

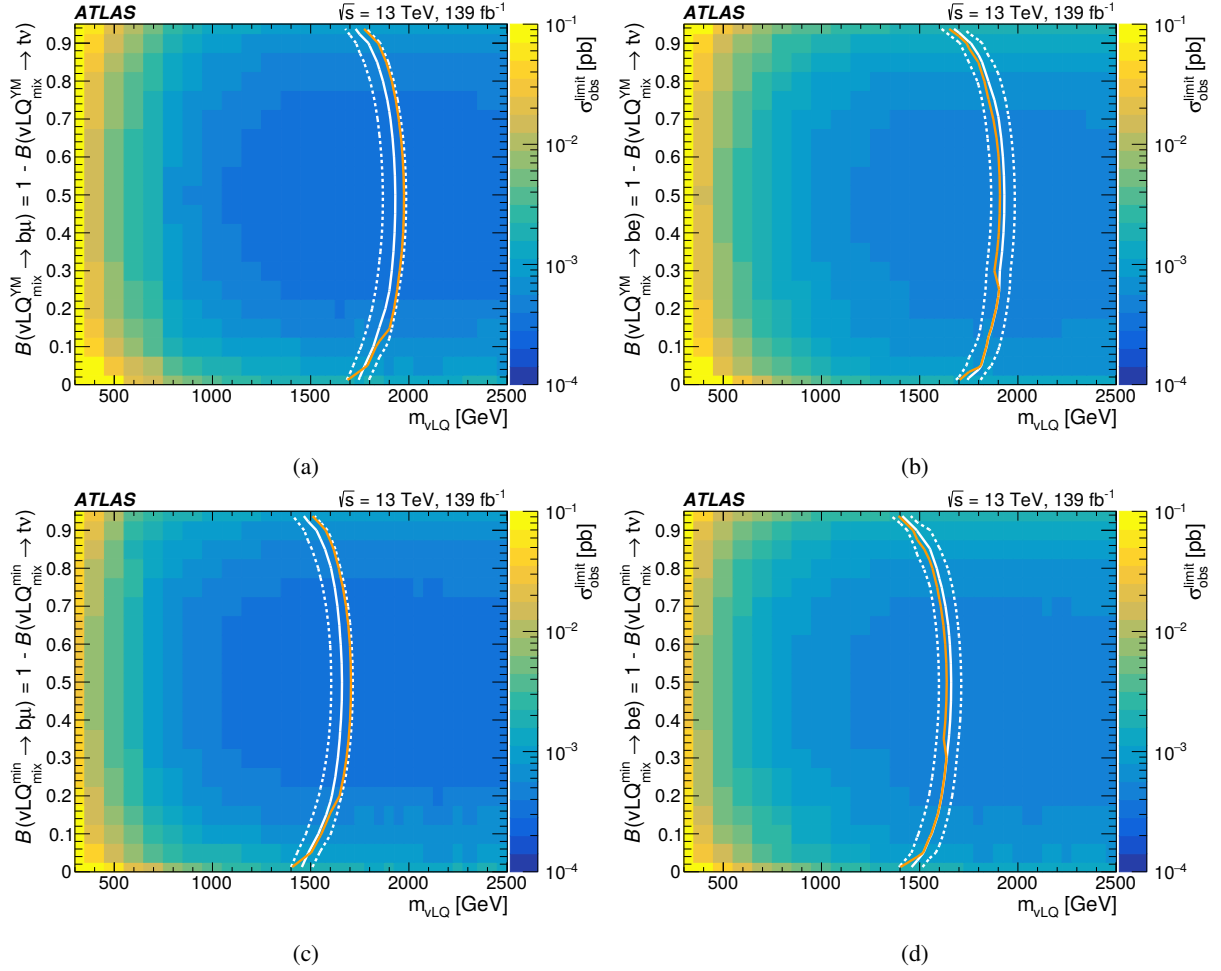


Figure 10: Expected (solid white, $\pm 1\sigma$ ranges dashed) and observed (solid red) exclusion limits on the leptoquark mass as a function of the branching ratio into charged leptons at 95% CL. The observed upper limit on the signal cross-section in each bin is shown on the z-axis. Limits are presented for (a) vector LQs in the Yang–Mills coupling scenario decaying into muons, (b) vector LQs in the Yang–Mills coupling scenario decaying into electrons, (c) vector LQs in the minimal coupling scenario decaying into muons, and (d) vector LQs in the minimal coupling scenario decaying into electrons.

a small deviation for the LQ_{mix}^u model at $\mathcal{B} = 0.0$, as already discussed above in the context of Figure 6. Differences between up- and down-type LQs can be observed especially for low values of \mathcal{B} , where events with $LQLQ \rightarrow t_{\text{lep}} \nu t_{\text{had}} \nu$ increase the sensitivity. The shapes of the exclusion limits for vector LQs with the Yang–Mills and the minimal coupling are very similar, since no significant kinematic differences exist at these higher masses. When comparing the limits for up-type scalar LQs with those for vector LQs, the kinematic differences due to spin correlations in $LQLQ \rightarrow t_{\text{lep}} \nu t_{\text{had}} \nu$ become relevant, i.e. when approaching $\mathcal{B} = 0.0$, the expected lower limit on the mass decreases faster for the vector LQ, as expected from Figure 4(b).

10 Conclusion

Results of a search for pair-produced scalar and vector leptoquarks decaying into quarks of the third generation and charged or neutral leptons of the first or second generation are presented, targeting the single-lepton final state. The analysis is based on data collected by the ATLAS experiment in $\sqrt{s} = 13$ TeV proton–proton collisions, corresponding to an integrated luminosity of 139 fb^{-1} . Several neural networks are trained for various signal hypotheses, covering a wide range of parameters. No significant deviations from the Standard Model expectation are observed and upper limits on the production cross-section are derived for eight models as a function of leptoquark mass and branching ratio into the charged lepton.

In addition, lower limits on the leptoquark mass are set across a range of branching ratios for all models. At a branching ratio of 0.5 they reach values of 1470 GeV (1440 GeV) for up-type scalar leptoquarks decaying into muons (electrons) and 1370 GeV (1390 GeV) for down-type scalar leptoquarks decaying into muons (electrons). For the first time, dedicated neural networks are used for U_1 vector leptoquarks, directly seeking an explanation for the various B -anomalies in a scenario where the leptoquark decays with similar branching fractions into either a charged or neutral lepton of the second generation, assuming couplings to quarks of only the third generation. The resulting lower limits on the mass are 1980 GeV and 1710 GeV for the Yang–Mills and the minimal coupling scenario, respectively. The decay into electrons is also probed and limits of 1900 GeV (1620 GeV) for the Yang–Mills (minimal) coupling scenario are calculated.

References

- [1] BaBar Collaboration, *Measurement of an excess of $\bar{B} \rightarrow D^{(*)}\tau^-\bar{\nu}_\tau$ decays and implications for charged Higgs bosons*, *Phys. Rev. D* **88** (2013) 072012, arXiv: [1303.0571](#).
- [2] Belle Collaboration, *Measurement of the branching ratio of $\bar{B} \rightarrow D^{(*)}\tau^-\bar{\nu}_\tau$ relative to $\bar{B} \rightarrow D^{(*)}\ell^-\bar{\nu}_\ell$ decays with hadronic tagging at Belle*, *Phys. Rev. D* **92** (2015) 072014, arXiv: [1507.03233](#).
- [3] LHCb Collaboration, *Measurement of the Ratio of Branching Fractions $\mathcal{B}(\bar{B}^0 \rightarrow D^{*+}\tau^-\bar{\nu}_\tau)/\mathcal{B}(\bar{B}^0 \rightarrow D^{*+}\mu^-\bar{\nu}_\mu)$* , *Phys. Rev. Lett.* **115** (2015) 111803, arXiv: [1506.08614](#),
Erratum: *Phys. Rev. Lett.* **115** (2015) 159901.
- [4] LHCb Collaboration, *Angular analysis of the $B^0 \rightarrow K^{*0}\mu^+\mu^-$ decay using 3 fb^{-1} of integrated luminosity*, *JHEP* **02** (2016) 104, arXiv: [1512.04442](#) [[hep-ex](#)].
- [5] Belle Collaboration, *Measurement of the τ Lepton Polarization and $R(D^*)$ in the Decay $\bar{B} \rightarrow D^*\tau^-\bar{\nu}_\tau$* , *Phys. Rev. Lett.* **118** (2017) 211801, arXiv: [1612.00529](#) [[hep-ex](#)].
- [6] Belle Collaboration, *Lepton-Flavor-Dependent Angular Analysis of $B \rightarrow K^*\ell^+\ell^-$* , *Phys. Rev. Lett.* **118** (2017) 111801, arXiv: [1612.05014](#) [[hep-ex](#)].
- [7] LHCb Collaboration, *Test of lepton universality with $B^0 \rightarrow K^{*0}\ell^+\ell^-$ decays*, *JHEP* **08** (2017) 055, arXiv: [1705.05802](#).
- [8] LHCb Collaboration, *Measurement of the Ratio of Branching Fractions $\mathcal{B}(B_c^+ \rightarrow J/\psi\tau^+\nu_\tau)/\mathcal{B}(B_c^+ \rightarrow J/\psi\mu^+\nu_\mu)$* , *Phys. Rev. Lett.* **120** (2018) 121801, arXiv: [1711.05623](#) [[hep-ex](#)].
- [9] LHCb Collaboration, *Test of lepton universality in beauty-quark decays*, *Nature Phys.* **18** (2022) 277, arXiv: [2103.11769](#) [[hep-ex](#)].
- [10] G. Hiller and M. Schmaltz, *R_K and future $b \rightarrow s\ell\ell$ physics beyond the standard model opportunities*, *Phys. Rev. D* **90** (2014) 054014, arXiv: [1408.1627](#) [[hep-ph](#)].
- [11] B. Gripaos, M. Nardecchia and S. A. Renner, *Composite leptoquarks and anomalies in B -meson decays*, *JHEP* **05** (2015) 006, arXiv: [1412.1791](#) [[hep-ph](#)].
- [12] M. Freytsis, Z. Ligeti and J. T. Ruderman, *Flavor models for $\bar{B} \rightarrow D^{(*)}\tau\bar{\nu}$* , *Phys. Rev. D* **92** (2015) 054018, arXiv: [1506.08896](#) [[hep-ph](#)].
- [13] M. Bauer and M. Neubert, *Minimal Leptoquark Explanation for the $R_{D^{(*)}}$, R_K , and $(g-2)_g$ Anomalies*, *Phys. Rev. Lett.* **116** (2016) 141802, arXiv: [1511.01900](#) [[hep-ph](#)].
- [14] L. Di Luzio and M. Nardecchia, *What is the scale of new physics behind the B -flavour anomalies?*, *Eur. Phys. J. C* **77** (2017) 536, arXiv: [1706.01868](#) [[hep-ph](#)].
- [15] D. Buttazzo, A. Greljo, G. Isidori and D. Marzocca, *B -physics anomalies: a guide to combined explanations*, *JHEP* **11** (2017) 044, arXiv: [1706.07808](#) [[hep-ph](#)].

- [16] J. M. Cline, *B decay anomalies and dark matter from vectorlike confinement*, [Phys. Rev. D **97** \(2018\) 015013](#), arXiv: [1710.02140 \[hep-ph\]](#).
- [17] E. C. Leskow, G. D'Ambrosio, A. Crivellin and D. Müller, *$(g - 2)_\mu$, lepton flavor violation, and Z decays with leptoquarks: Correlations and future prospects*, [Phys. Rev. D **95** \(2017\) 055018](#), arXiv: [1612.06858 \[hep-ph\]](#).
- [18] D. Chakraverty, D. Choudhury and A. Datta, *A nonsupersymmetric resolution of the anomalous muon magnetic moment*, [Phys. Lett. B **506** \(2001\) 103](#), arXiv: [hep-ph/0102180](#).
- [19] Muon $g - 2$ Collaboration, *Measurement of the Positive Muon Anomalous Magnetic Moment to 0.46 ppm*, [Phys. Rev. Lett. **126** \(2021\) 141801](#), arXiv: [2104.03281 \[hep-ex\]](#).
- [20] H. Georgi and S. Glashow, *Unity of All Elementary Particle Forces*, [Phys. Rev. Lett. **32** \(1974\) 438](#).
- [21] J. C. Pati and A. Salam, *Lepton number as the fourth "color"*, [Phys. Rev. D **10** \(1974\) 275](#).
- [22] W. Buchmüller and D. Wyler, *Constraints on SU(5)-type leptoquarks*, [Phys. Lett. B **177** \(1986\) 377](#).
- [23] S. Dimopoulos and L. Susskind, *Mass without scalars*, [Nucl. Phys. B **155** \(1979\) 237](#).
- [24] S. Dimopoulos, *Technicoloured signatures*, [Nucl. Phys. B **168** \(1980\) 69](#).
- [25] E. Eichten and K. Lane, *Dynamical breaking of weak interaction symmetries*, [Phys. Lett. B **90** \(1980\) 125](#).
- [26] L. F. Abbott and E. Farhi, *Are the weak interactions strong?*, [Phys. Lett. B **101** \(1981\) 69](#).
- [27] L. F. Abbott and E. Farhi, *A confining model of the weak interactions*, [Nucl. Phys. B **189** \(1981\) 547](#).
- [28] B. Schrempp and F. Schrempp, *Light leptoquarks*, [Phys. Lett. B **153** \(1985\) 101](#).
- [29] W. Buchmüller, R. Rückl and D. Wyler, *Leptoquarks in lepton - quark collisions*, [Phys. Lett. B **191** \(1987\) 442](#), Erratum: [Phys. Lett. B **448** \(1999\) 320](#).
- [30] R. Alonso, B. Grinstein and J. Martin Camalich, *Lepton universality violation and lepton flavor conservation in B-meson decays*, [JHEP **10** \(2015\) 184](#), arXiv: [1505.05164 \[hep-ph\]](#).
- [31] R. Barbieri, G. Isidori, A. Pattori and F. Senia, *Anomalies in B-decays and U(2) flavor symmetry*, [Eur. Phys. J. C **76** \(2016\) 67](#), arXiv: [1512.01560 \[hep-ph\]](#).
- [32] ATLAS Collaboration, *Search for pair production of scalar leptoquarks decaying into first- or second-generation leptons and top quarks in proton-proton collisions at $\sqrt{s} = 13$ TeV with the ATLAS detector*, [Eur. Phys. J. C **81** \(2021\) 313](#), arXiv: [2010.02098 \[hep-ex\]](#).
- [33] ATLAS Collaboration, *Search for pairs of scalar leptoquarks decaying into quarks and electrons or muons in $\sqrt{s} = 13$ TeV pp collisions with the ATLAS detector*, [JHEP **10** \(2020\) 112](#), arXiv: [2006.05872 \[hep-ex\]](#).
- [34] CMS Collaboration, *Search for Leptoquarks Coupled to Third-Generation Quarks in Proton-Proton Collisions at $\sqrt{s} = 13$ TeV*, [Phys. Rev. Lett. **121** \(2018\) 241802](#), arXiv: [1809.05558 \[hep-ex\]](#).

- [35] T. Mandal, S. Mitra and S. Seth, *Pair production of scalar leptoquarks at the LHC to NLO parton shower accuracy*, *Phys. Rev. D* **93** (2016) 035018, arXiv: [1506.07369 \[hep-ph\]](#).
- [36] ATLAS Collaboration, *Searches for third-generation scalar leptoquarks in $\sqrt{s} = 13$ TeV pp collisions with the ATLAS detector*, *JHEP* **06** (2019) 144, arXiv: [1902.08103 \[hep-ex\]](#).
- [37] M. J. Baker, J. Fuentes-Martín, G. Isidori and M. König, *High- p_T signatures in vector-leptoquark models*, *Eur. Phys. J. C* **79** (2019) 334, arXiv: [1901.10480 \[hep-ph\]](#).
- [38] ATLAS Collaboration, *The ATLAS Experiment at the CERN Large Hadron Collider*, *JINST* **3** (2008) S08003.
- [39] ATLAS Collaboration, *The ATLAS Collaboration Software and Firmware*, ATL-SOFT-PUB-2021-001, 2021, URL: <https://cds.cern.ch/record/2767187>.
- [40] ATLAS Collaboration, *ATLAS data quality operations and performance for 2015–2018 data-taking*, *JINST* **15** (2020) P04003, arXiv: [1911.04632 \[physics.ins-det\]](#).
- [41] E. Bothmann et al., *Event generation with Sherpa 2.2*, *SciPost Phys.* **7** (2019) 034, arXiv: [1905.09127 \[hep-ph\]](#).
- [42] D. J. Lange, *The EvtGen particle decay simulation package*, *Nucl. Instrum. Meth. A* **462** (2001) 152.
- [43] T. Sjöstrand, S. Mrenna and P. Skands, *A brief introduction to PYTHIA 8.1*, *Comput. Phys. Commun.* **178** (2008) 852, arXiv: [0710.3820 \[hep-ph\]](#).
- [44] ATLAS Collaboration, *The Pythia 8 A3 tune description of ATLAS minimum bias and inelastic measurements incorporating the Donnachie–Landshoff diffractive model*, ATL-PHYS-PUB-2016-017, 2016, URL: <https://cds.cern.ch/record/2206965>.
- [45] ATLAS Collaboration, *The ATLAS Simulation Infrastructure*, *Eur. Phys. J. C* **70** (2010) 823, arXiv: [1005.4568 \[physics.ins-det\]](#).
- [46] GEANT4 Collaboration, S. Agostinelli et al., *GEANT4 – a simulation toolkit*, *Nucl. Instrum. Meth. A* **506** (2003) 250.
- [47] J. Alwall et al., *The automated computation of tree-level and next-to-leading order differential cross sections, and their matching to parton shower simulations*, *JHEP* **07** (2014) 079, arXiv: [1405.0301 \[hep-ph\]](#).
- [48] R. D. Ball et al., *Parton distributions for the LHC run II*, *JHEP* **04** (2015) 040, arXiv: [1410.8849 \[hep-ph\]](#).
- [49] M. Krämer, T. Plehn, M. Spira and P. M. Zerwas, *Pair production of scalar leptoquarks at the CERN LHC*, *Phys. Rev. D* **71** (2005) 057503, arXiv: [hep-ph/0411038](#).
- [50] M. Krämer, T. Plehn, M. Spira and P. M. Zerwas, *Pair Production of Scalar Leptoquarks at the Fermilab Tevatron*, *Phys. Rev. Lett.* **79** (1997) 341, arXiv: [hep-ph/9704322](#).
- [51] P. Artoisenet, R. Frederix, O. Mattelaer and R. Rietkerk, *Automatic spin-entangled decays of heavy resonances in Monte Carlo simulations*, *JHEP* **03** (2013) 015, arXiv: [1212.3460 \[hep-ph\]](#).

- [52] T. Sjöstrand et al., *An introduction to PYTHIA 8.2*, *Comput. Phys. Commun.* **191** (2015) 159, arXiv: [1410.3012 \[hep-ph\]](#).
- [53] ATLAS Collaboration, *ATLAS Pythia 8 tunes to 7 TeV data*, ATL-PHYS-PUB-2014-021, 2014, URL: <https://cds.cern.ch/record/1966419>.
- [54] R. D. Ball et al., *Parton distributions with LHC data*, *Nucl. Phys. B* **867** (2013) 244, arXiv: [1207.1303 \[hep-ph\]](#).
- [55] W. Beenakker, C. Borschensky, M. Krämer, A. Kulesza and E. Laenen, *NNLL-fast: predictions for coloured supersymmetric particle production at the LHC with threshold and Coulomb resummation*, *JHEP* **12** (2016) 133, arXiv: [1607.07741 \[hep-ph\]](#).
- [56] W. Beenakker, M. Krämer, T. Plehn, M. Spira and P. M. Zerwas, *Stop production at hadron colliders*, *Nucl. Phys. B* **515** (1998) 3, arXiv: [hep-ph/9710451](#).
- [57] W. Beenakker et al., *Supersymmetric top and bottom squark production at hadron colliders*, *JHEP* **08** (2010) 098, arXiv: [1006.4771 \[hep-ph\]](#).
- [58] W. Beenakker et al., *NNLL resummation for stop pair-production at the LHC*, *JHEP* **05** (2016) 153, arXiv: [1601.02954 \[hep-ph\]](#).
- [59] C. Borschensky, B. Fuks, A. Kulesza and D. Schwartländer, *Scalar leptoquark pair production at hadron colliders*, *Phys. Rev. D* **101** (2020) 115017, arXiv: [2002.08971 \[hep-ph\]](#).
- [60] URL: <https://feynrules.irmp.ucl.ac.be/wiki/LeptoQuark>.
- [61] S. Frixione, G. Ridolfi and P. Nason, *A positive-weight next-to-leading-order Monte Carlo for heavy flavour hadroproduction*, *JHEP* **09** (2007) 126, arXiv: [0707.3088 \[hep-ph\]](#).
- [62] P. Nason, *A new method for combining NLO QCD with shower Monte Carlo algorithms*, *JHEP* **11** (2004) 040, arXiv: [hep-ph/0409146](#).
- [63] S. Frixione, P. Nason and C. Oleari, *Matching NLO QCD computations with parton shower simulations: the POWHEG method*, *JHEP* **11** (2007) 070, arXiv: [0709.2092 \[hep-ph\]](#).
- [64] S. Alioli, P. Nason, C. Oleari and E. Re, *A general framework for implementing NLO calculations in shower Monte Carlo programs: the POWHEG BOX*, *JHEP* **06** (2010) 043, arXiv: [1002.2581 \[hep-ph\]](#).
- [65] ATLAS Collaboration, *Studies on top-quark Monte Carlo modelling for Top2016*, ATL-PHYS-PUB-2016-020, 2016, URL: <https://cds.cern.ch/record/2216168>.
- [66] M. Czakon and A. Mitov, *Top++: A program for the calculation of the top-pair cross-section at hadron colliders*, *Comput. Phys. Commun.* **185** (2014) 2930, arXiv: [1112.5675 \[hep-ph\]](#).
- [67] S. Frixione, E. Laenen, P. Motylinski, C. White and B. R. Webber, *Single-top hadroproduction in association with a W boson*, *JHEP* **07** (2008) 029, arXiv: [0805.3067 \[hep-ph\]](#).
- [68] T. Gleisberg and S. Höche, *Comix, a new matrix element generator*, *JHEP* **12** (2008) 039, arXiv: [0808.3674 \[hep-ph\]](#).
- [69] F. Cascioli, P. Maierhöfer and S. Pozzorini, *Scattering Amplitudes with Open Loops*, *Phys. Rev. Lett.* **108** (2012) 111601, arXiv: [1111.5206 \[hep-ph\]](#).

- [70] A. Denner, S. Dittmaier and L. Hofer, *COLLIER: A fortran-based complex one-loop library in extended regularizations*, *Comput. Phys. Commun.* **212** (2017) 220, arXiv: [1604.06792 \[hep-ph\]](#).
- [71] S. Schumann and F. Krauss, *A parton shower algorithm based on Catani–Seymour dipole factorisation*, *JHEP* **03** (2008) 038, arXiv: [0709.1027 \[hep-ph\]](#).
- [72] S. Höche, F. Krauss, M. Schönherr and F. Siegert, *A critical appraisal of NLO+PS matching methods*, *JHEP* **09** (2012) 049, arXiv: [1111.1220 \[hep-ph\]](#).
- [73] S. Höche, F. Krauss, M. Schönherr and F. Siegert, *QCD matrix elements + parton showers. The NLO case*, *JHEP* **04** (2013) 027, arXiv: [1207.5030 \[hep-ph\]](#).
- [74] S. Catani, F. Krauss, B. R. Webber and R. Kuhn, *QCD Matrix Elements + Parton Showers*, *JHEP* **11** (2001) 063, arXiv: [hep-ph/0109231](#).
- [75] S. Höche, F. Krauss, S. Schumann and F. Siegert, *QCD matrix elements and truncated showers*, *JHEP* **05** (2009) 053, arXiv: [0903.1219 \[hep-ph\]](#).
- [76] C. Anastasiou, L. Dixon, K. Melnikov and F. Petriello, *High-precision QCD at hadron colliders: Electroweak gauge boson rapidity distributions at next-to-next-to leading order*, *Phys. Rev. D* **69** (2004) 094008, arXiv: [hep-ph/0312266](#).
- [77] ATLAS Collaboration, *Electron and photon performance measurements with the ATLAS detector using the 2015–2017 LHC proton–proton collision data*, *JINST* **14** (2019) P12006, arXiv: [1908.00005 \[hep-ex\]](#).
- [78] ATLAS Collaboration, *Muon reconstruction and identification efficiency in ATLAS using the full Run 2 pp collision data set at $\sqrt{s} = 13$ TeV*, *Eur. Phys. J. C* **81** (2021) 578, arXiv: [2012.00578 \[hep-ex\]](#).
- [79] ATLAS Collaboration, *Jet reconstruction and performance using particle flow with the ATLAS Detector*, *Eur. Phys. J. C* **77** (2017) 466, arXiv: [1703.10485 \[hep-ex\]](#).
- [80] ATLAS Collaboration, *Jet energy scale and resolution measured in proton–proton collisions at $\sqrt{s} = 13$ TeV with the ATLAS detector*, *Eur. Phys. J. C* **81** (2020) 689, arXiv: [2007.02645 \[hep-ex\]](#).
- [81] M. Cacciari, G. P. Salam and G. Soyez, *The anti- k_t jet clustering algorithm*, *JHEP* **04** (2008) 063, arXiv: [0802.1189 \[hep-ph\]](#).
- [82] M. Cacciari, G. P. Salam and G. Soyez, *FastJet user manual*, *Eur. Phys. J. C* **72** (2012) 1896, arXiv: [1111.6097 \[hep-ph\]](#).
- [83] ATLAS Collaboration, *Tagging and suppression of pileup jets with the ATLAS detector*, ATLAS-CONF-2014-018, 2014, URL: <https://cds.cern.ch/record/1700870>.
- [84] ATLAS Collaboration, *ATLAS b-jet identification performance and efficiency measurement with $\bar{t}\bar{t}$ events in pp collisions at $\sqrt{s} = 13$ TeV*, *Eur. Phys. J. C* **79** (2019) 970, arXiv: [1907.05120 \[hep-ex\]](#).
- [85] ATLAS Collaboration, *Optimisation and performance studies of the ATLAS b-tagging algorithms for the 2017-18 LHC run*, ATL-PHYS-PUB-2017-013, 2017, URL: <https://cds.cern.ch/record/2273281>.

- [86] ATLAS Collaboration, *Search for top-squark pair production in final states with one lepton, jets, and missing transverse momentum using 36fb^{-1} of $\sqrt{s} = 13\text{ TeV}$ pp collision data with the ATLAS detector*, [JHEP **06** \(2018\) 108](#), arXiv: [1711.11520 \[hep-ex\]](#).
- [87] ATLAS Collaboration, *Performance of missing transverse momentum reconstruction with the ATLAS detector using proton–proton collisions at $\sqrt{s} = 13\text{ TeV}$* , [Eur. Phys. J. C **78** \(2018\) 903](#), arXiv: [1802.08168 \[hep-ex\]](#).
- [88] ATLAS Collaboration, *Performance of the missing transverse momentum triggers for the ATLAS detector during Run-2 data taking*, [JHEP **08** \(2020\) 080](#), arXiv: [2005.09554 \[hep-ex\]](#).
- [89] ATLAS Collaboration, *Measurement of the $t\bar{t}$ production cross-section and lepton differential distributions in $e\mu$ dilepton events from pp collisions at $\sqrt{s} = 13\text{ TeV}$ with the ATLAS detector*, [Eur. Phys. J. C **80** \(2020\) 528](#), arXiv: [1910.08819 \[hep-ex\]](#).
- [90] ATLAS Collaboration, *Measurements of top-quark pair differential and double-differential cross-sections in the ℓ +jets channel with pp collisions at $\sqrt{s} = 13\text{ TeV}$ using the ATLAS detector*, [Eur. Phys. J. C **79** \(2019\) 1028](#), arXiv: [1908.07305 \[hep-ex\]](#),
Erratum: [Eur. Phys. J. C **80** \(2020\) 1092](#).
- [91] C. Lester and D. Summers, *Measuring masses of semi-invisibly decaying particle pairs produced at hadron colliders*, [Phys. Lett. B **463** \(1999\) 99](#), arXiv: [hep-ph/9906349](#).
- [92] A. J. Barr, B. Gripaios and C. G. Lester, *Transverse masses and kinematic constraints: from the boundary to the crease*, [JHEP **11** \(2009\) 096](#), arXiv: [0908.3779 \[hep-ph\]](#).
- [93] Y. Bai, H.-C. Cheng, J. Gallicchio and J. Gu, *Stop the top background of the stop search*, [JHEP **07** \(2012\) 110](#), arXiv: [1203.4813 \[hep-ph\]](#).
- [94] M. Feindt, *A Neural Bayesian Estimator for Conditional Probability Densities*, 2004, arXiv: [physics/0402093 \[physics.data-an\]](#).
- [95] M. Feindt and U. Kerzel, *The NeuroBayes Neural Network Package*, [Nucl. Instrum. Meth. A **559** \(2006\) 190](#).
- [96] ATLAS Collaboration, *Studies of $t\bar{t}/tW$ interference effects in $b\bar{b}\ell^+\ell'^-\nu\bar{\nu}'$ final states with POWHEG and MADGRAPH5_AMC@NLO setups*, ATL-PHYS-PUB-2021-042, 2021, URL: <https://cds.cern.ch/record/2792254>.
- [97] J. Bellm et al., *Herwig 7.1 Release Note*, (2017), arXiv: [1705.06919 \[hep-ph\]](#).
- [98] J. Butterworth et al., *PDF4LHC recommendations for LHC Run II*, [J. Phys. G **43** \(2016\) 023001](#), arXiv: [1510.03865 \[hep-ph\]](#).
- [99] E. Re, *Single-top Wt -channel production matched with parton showers using the POWHEG method*, [Eur. Phys. J. C **71** \(2011\) 1547](#), arXiv: [1009.2450 \[hep-ph\]](#).
- [100] ATLAS Collaboration, *Multi-boson simulation for 13 TeV ATLAS analyses*, ATL-PHYS-PUB-2016-002, 2016, URL: <https://cds.cern.ch/record/2119986>.
- [101] ATLAS Collaboration, *Measurement of W^\pm and Z-boson production cross sections in pp collisions at $\sqrt{s} = 13\text{ TeV}$ with the ATLAS detector*, [Phys. Lett. B **759** \(2016\) 601](#), arXiv: [1603.09222 \[hep-ex\]](#).

- [102] D. de Florian et al., *Handbook of LHC Higgs Cross Sections: 4. Deciphering the Nature of the Higgs Sector*, (2016), arXiv: [1610.07922 \[hep-ph\]](#).
- [103] ATLAS Collaboration, *Measurement of the $t\bar{t}Z$ and $t\bar{t}W$ cross sections in proton–proton collisions at $\sqrt{s} = 13$ TeV with the ATLAS detector*, *Phys. Rev. D* **99** (2019) 072009, arXiv: [1901.03584 \[hep-ex\]](#).
- [104] ATLAS Collaboration, *E_T^{miss} performance in the ATLAS detector using 2015–2016 LHC pp collisions*, ATLAS-CONF-2018-023, 2018, URL: <https://cds.cern.ch/record/2625233>.
- [105] ATLAS Collaboration, *Luminosity determination in pp collisions at $\sqrt{s} = 13$ TeV using the ATLAS detector at the LHC*, ATLAS-CONF-2019-021, 2019, URL: <https://cds.cern.ch/record/2677054>.
- [106] G. Avoni et al., *The new LUCID-2 detector for luminosity measurement and monitoring in ATLAS*, *JINST* **13** (2018) P07017.
- [107] W. Verkerke and D. Kirkby, *The RooFit toolkit for data modeling*, 2003, arXiv: [physics/0306116 \[physics.data-an\]](#).
- [108] A. L. Read, *Presentation of search results: the CL_S technique*, *J. Phys. G* **28** (2002) 2693.
- [109] G. Cowan, K. Cranmer, E. Gross and O. Vitells, *Asymptotic formulae for likelihood-based tests of new physics*, *Eur. Phys. J. C* **71** (2011) 1554, arXiv: [1007.1727 \[physics.data-an\]](#), Erratum: *Eur. Phys. J. C* **73** (2013) 2501.